

The Detection and Characterization of Be+sdO Binaries from HST/STIS FUV Spectroscopy

LUQIAN WANG,^{1,2} DOUGLAS R. GIES,¹ GERALDINE J. PETERS,³ YLVA GÖTBERG,⁴
S. DREW CHOJNOWSKI,⁵ KATHRYN V. LESTER,⁶ AND STEVE B. HOWELL⁶

¹*Center for High Angular Resolution Astronomy and Department of Physics and Astronomy
Georgia State University, P.O. Box 5060*

Atlanta, GA 30302-5060, USA

²*Yunnan Observatories, CAS, P.O. Box 110, Kunming 650011, Yunnan, China*

³*Space Science Center, Department of Physics and Astronomy, University of Southern California, Los Angeles, CA
90089-1341, USA*

⁴*Carnegie Observatories, 813 Santa Barbara Street, Pasadena, CA 91101, USA*

⁵*Apache Point Observatory and New Mexico State University, P.O. Box 59, Sunspot, NM 88349-0059, USA*

⁶*NASA Ames Research Center, Moffett Field, CA 94035, USA*

(Revised March 20, 2021; Accepted March 23, 2021)

Submitted to AJ

ABSTRACT

The B-emission line stars are rapid rotators that were probably spun up by mass and angular momentum accretion through mass transfer in an interacting binary. Mass transfer will strip the donor star of its envelope to create a small and hot subdwarf remnant. Here we report on *Hubble Space Telescope* / STIS far-ultraviolet spectroscopy of a sample of Be stars that reveals the presence of the hot sdO companion through the calculation of cross-correlation functions of the observed and model spectra. We clearly detect the spectral signature of the sdO star in 10 of the 13 stars in the sample, and the spectral signals indicate that the sdO stars are hot, relatively faint, and slowly rotating as predicted by models. A comparison of their temperatures and radii with evolutionary tracks indicates that the sdO stars occupy the relatively long-lived, He-core burning stage. Only one of the ten detections was a known binary prior to this investigation, which emphasizes the difficulty of finding such Be+sdO binaries through optical spectroscopy. However, these results and others indicate that many Be stars probably host hot subdwarf companions.

Keywords: binaries: spectroscopic — stars: emission-line, Be — stars: evolution — subdwarfs

1. INTRODUCTION

Close binaries are common among massive stars, and growing evidence suggests that many massive stars are evolutionary products of post-interacting binary systems that have experienced mass transfer (de Mink et al. 2014). There are two main routes of binary interaction. In the case where the companion star has much lower mass, the more massive component will evolve and fill its Roche lobe, and may engulf the companion in a common envelope stage that leads to a merger. Alternatively, for systems with more comparable masses, the more massive, donor star will transfer its mass and angular momentum to the gainer star through Roche lobe overflow. The orbit shrinks and promotes further mass transfer until the two components reach comparable masses. Then continuing mass transfer will expand the orbit until the donor star is stripped of its outer envelope, leaving a hot core with a size much smaller than its Roche lobe. The gainer star will become a rapid rotator.

Be stars are B-type main sequence stars, and their optical spectra display broad $H\alpha$ emission that originates in an outflowing, circumstellar decretion disk. They are rapidly rotating stars, and their projected rotational velocities $V \sin i$ can reach up to 70 to 80% or larger of their critical rotational velocities (Yudin 2001; Huang et al. 2010). Pols et al. (1991) and Shao & Li (2014) argue that Be stars were spun up through close binary interactions. If so, then many Be stars will have companions that are the remnants of the mass donor. The final stripped donor star may explode to create a neutron star in a Be X-ray binary, or it will evolve into a faint, hot, low-mass subdwarf (sdO) star and create a Be+sdO binary system. Pols et al. (1991) predict that majority of the evolved companions in Be binaries are He stars (sdO remnants). Recently Bodensteiner et al.

(2020a) showed that Be stars lack normal B-type companions, in stark contrast to regular B-type stars, and they argue that this implies that many Be stars are the products of binary interaction (either mergers or binaries with faint evolved companions).

The sdO spectral designation encompasses a wide range of hot objects with diverse evolutionary histories. Many sdO stars occupy the extreme horizontal branch in the H-R diagram, and they typically have effective temperatures in the range of 35 kK to 55 kK, gravities $\log g$ spanning the range of 5.1 and 6.4 (c.g.s units), and luminosities from 10 to 100 times solar luminosity (Heber 2009, 2016). Most of the sdO stars are probably descendants of red giant stars, although some have hot temperatures and high luminosities similar to those of the central stars of planetary nebulae (Heber et al. 1988; Rauch et al. 1991). The sdO stars with temperatures below 40 kK are probably He-core burning objects, while the hotter ones have entered a subsequent He-shell burning stage. The sdO companions of Be stars must have formed by stripping through binary interactions, and they typically have larger masses and radii than the general population of low-mass sdO stars.

The sdO components of Be binary systems are faint and hard to detect, but they are hot and contribute more flux in the shorter wavelength part of the spectrum due to their high temperature. Thus, searches for their spectral features are more favorable in the far-ultraviolet (FUV). The first detection of the spectrum of an sdO star in a Be binary ϕ Per was reported by Thaller et al. (1995) using the *International Ultraviolet Explorer (IUE)* FUV spectroscopy. They estimated that the sdO companion contributes $\sim 12\%$ of the UV flux of the Be star. This result was confirmed by Gies et al. (1998) from FUV observations with *Hubble Space Telescope (HST)*, and the sdO-to-Be flux ratio was estimated to be 16% at 1374 Å. The binary

orbit of this system was subsequently resolved through long baseline interferometry with the CHARA Array by Mourard et al. (2015). Continuing searches for sdO companion stars using *IUE* spectroscopy led to the discovery of another three Be+sdO systems: FY CMa (Peters et al. 2008), 59 Cyg (Peters et al. 2013), and 60 Cyg (Wang et al. 2017). The sdO companions in these systems contribute $\sim 4\%$ of the FUV flux. One fainter sdO companion was found in HR 2142, which has an estimated flux ratio of only $\sim 1\%$ (Peters et al. 2016). Wang et al. (2018) conducted an *IUE* survey study to search for additional Be+sdO systems, and they found another 12 candidates in a sample of 264 stars that were not known binaries. Chojnowski et al. (2018) reported a detection of a sdO companion through an investigation of a large set of optical spectra in Be binary system HD 55606, and several other systems are suspected of hosting a hot companion from clues in their optical spectra (Koubský et al. 2012, 2014; Harmanec et al. 2020). The detected sdO companions have temperatures in the range of 42 to 53 kK and masses between 0.7 and 1.7 M_{\odot} .

These Be+sdO binaries are important for studies of massive star evolution, because a large fraction of massive stars have nearby stellar companions (Sana et al. 2012) and binary interactions play a key role in their destinies (de Mink et al. 2014). Hot sdO stars may contribute significantly to the UV flux of stellar populations (Han et al. 2010; Götzberg et al. 2019) and constitute an important contribution to spectral synthesis models (Eldridge et al. 2017). Those sdO stars with a mass above the Chandrasekhar limit may explode as hydrogen deficient supernovae (SN Ib and SN Ic; Eldridge et al. 2013). Binary systems at the high mass end may also be closely related to the progenitors of neutron star pairs that can merge to create bright gravitational wave sources (Tauris et al. 2017).

Be+sdO binaries may also be related to several systems that are claimed to be black hole binaries. Liu et al. (2019) found that the LB-1 system consists of what appears to be a B-giant star with an invisible companion. More recently, Rivinius et al. (2020) reported that HR 6819 also hosts a B-giant orbiting an unseen companion. In both cases, the mass of the faint component is much larger than that of the B-giant, so that the companions are possibly black holes but without the X-ray emission that characterizes the massive X-ray binaries. Also, in both cases Balmer line emission is present, the defining criterion of Be stars. Subsequent work indicates that both the emission lines (Liu et al. 2020; Gies & Wang 2020) and faint, broad absorption lines (Shenar et al. 2020; Bodensteiner et al. 2020b; El-Badry & Quataert 2021) show the small-amplitude, reflex orbital motion around the B-giant component. If the Be star component has normal mass, then the B-giant component must be an unusual, low mass object. Furthermore, the atmosphere of the B-giant component in LB-1 is enriched in He and N (Irrgang et al. 2020; Shenar et al. 2020), and a N enrichment is found for HR 6819 (Bodensteiner et al. 2020b; El-Badry & Quataert 2021). These enrichments are associated with He-core burning through the CNO-cycle, and their presence suggests that plasma from the core now occupies their atmospheres. Thus, the B-giant star in both cases may be the stripped remnant of mass transfer caught during a short transition stage leading to a Be+sdO system (Section 7).

It is vitally important to obtain FUV spectroscopy of Be+sdO systems, because analysis of their rich spectra offers us the means to determine the physical parameters of the stripped-down remnants. Here we report on new FUV spectroscopy from the *HST* / Space Telescope Imaging Spectrograph (STIS) of the sample of candidate Be+sdO binaries from the work of

Wang et al. (2018) and Chojnowski et al. (2018). We describe the FUV observations and associated reduction details in Section 2. In Section 3, we present measurements of the radial velocities of the Be stars. These are used in Section 4 to remove the Be star contribution to cross-correlation functions (CCFs) of the observed spectrum with a model spectrum for the hot component. We detect the CCF signal from a hot sdO component in 10 of the 13 systems. In Section 5, we describe our methodology to determine the physical properties of the sdO stars for the detections. We use model fits of the observed spectral energy distributions in Section 6 to determine the angular diameters of the Be stars, and these are used with the estimated distances and radius ratios to estimate the radii of each stellar component. Section 7 presents a comparison of the derived temperatures and radii of the sdO components with evolutionary tracks. We summarize our work in Section 8.

2. *HST*/STIS FUV SPECTROSCOPY

The targets of this investigation were identified as candidate Be+sdO binaries by Wang et al. (2018) through an examination of cross-correlation functions (CCFs) of high dispersion, Short Wavelength Prime (SWP) camera spectra from *IUE* with a model spectrum with an assumed temperature of 45 kK. These 12 targets all displayed narrow CCF peaks (unlike the broader Be star features), and the CCF peaks were generally velocity variable (in cases with multiple spectra), indicating Doppler shifts from orbital motion. The final target HD 55606 was discovered to be a Be+sdO binary with a 93.76 day period by Chojnowski et al. (2018), who observed narrow components of He I lines from the sdO component in high quality optical spectra. Table 1 summarizes the properties of the sample. It lists the Henry Draper Memorial (HD) catalog number, star name, spectral classification, and physical properties of the Be stars, including the effective temperature (T_{eff}),

gravity ($\log g$), and projected rotational velocity ($V \sin i$), as well as source references for these estimates. We also include in last column an estimate of $V \sin i$ that we applied in creating models of the Be star spectrum to account for its contribution to the CCF analysis (see Section 4).

We obtained FUV spectra of the 13 Be+sdO candidate systems with the *Hubble Space Telescope* and Space Telescope Imaging Spectrograph (STIS) (Kimble et al. 1998). The spectra were made with the MAMA detector and the E140M echelle grating. The spectra cover a wavelength range of 1144 – 1710 Å with a resolving power of $R = 45,800$ (Riley et al. 2019). Most of the stars are bright and required the use of the 0.2X0.05ND or other aperture with a neutral density filter in order to meet the bright flux limits of the MAMA detector. The sole exception was the fainter star, HD 55606, where the default 0.2X0.2 aperture was used. The observations were made for each target in three, single orbit visits between 2019 August and 2020 February at intervals of days to months. We usually obtained a signal-to-noise ratio of 30 per pixel or better in the best exposed parts of the spectrum.

The FUV spectra were reduced, and the wavelength and flux were calibrated, following the standard STIS pipeline (Sohn et al. 2019). We subsequently combined the echelle orders onto a single uniform wavelength grid on a $\log \lambda$ scale with an equivalent pixel size of 7.5 km s^{-1} . A number of prominent interstellar medium lines, such as Si IV $\lambda\lambda 1394, 1403$, and C IV $\lambda\lambda 1548, 1550$, were removed from the spectra by linear interpolation across the features. We also removed the geocoronal Ly α $\lambda 1216$ line by interpolation. The spectra were rectified in flux by applying a spline fit to relatively line-free regions. The final working product was a rectified spectrum matrix as a function of wavelength and heliocentric Julian date (HJD). Figure 1

Table 1. List of targets

HD Number	Star Name	Spectral Classification	Reference	T_{eff} (K)	Reference	$\log g$ (cm s^{-2})	Reference	$V \sin i$ (km s^{-1})	Reference	$V \sin i$ (km s^{-1})
29441	V1150 Tau	B2.5 Vne	1	20350	2	4.0	11	338	3	380
43544	HR 2249	B3 V	1	21500	4	3.9	4	260	7	260
51354	QY Gem	B3 Ve	1	20000	11	4.0	11	330	5	330
55606	MWC 522	B2 Vnnpe	6	27350	7	4.3	7	335	7	335
60855	V378 Pup	B3 IV	1	20000	11	4.0	11	244	8	300
113120	LS Mus	B2 IVne	4	22800	7	3.7	7	339	7	460
137387	κ Aps	B2 Vnpe	4	23950	7	4.0	7	250	7	380
152478	V846 Ara	B3 Vnpe	4	19800	7	3.7	7	295	7	300
157042	ι Ara	B2.5 IVe	1	25860	7	4.2	7	340	7	320
157832	V750 Ara	B1.5 Ve	9	25000	9	3.9	11	277	10	250
191610	28 Cyg	B3 IVe	1	20470	7	3.7	7	300	7	300
194335	V2119 Cyg	B2 IIIe	1	25600	7	4.3	7	360	7	360
214168	8 Lac A	B1 IVe	1	27380	7	4.1	7	300	7	360

NOTE—Indices of references: (1) Slettebak (1982) (2) Hohle et al. (2010) (3) Jaschek & Egret (1982) (4) Levenhagen & Leister (2006) (5) Halbedel (1996) (6) Chojnowski et al. (2018) (7) Zorec et al. (2016) (8) Huang & Gies (2006) (9) Lopes de Oliveira & Motch (2011) (10) Yudin (2001) (11) Estimated values based upon spectral classification.

displays the observed spectra of a cooler Be star (HD 43544) and a hotter Be star (HD 55606). The observed spectrum is shown in black, and it is compared to model spectra for the Be star (offset by +1.0 and shown in blue) and the sdO star (offset by +2.5 and shown in green). These kinds of models are used in the CCF analyses described below (see Sections 3 and 4).

3. RADIAL VELOCITIES OF THE Be STARS

Our main goal in this work is to find the spectral line patterns that correspond to the faint, sdO companion star in these targets. It is very difficult to identify individual spectral lines from the sdO star because they are weak in the combined spectrum and blended with the rotationally broadened lines of the Be star. Instead, we calculate the cross-correlation functions (CCFs) of the observed spectra with a model spectrum for an adopted hot temperature for the sdO star. The CCF effectively multiplexes the spectral signal from all the faint lines into a single high S/N CCF for investigation. However, there is usually some correlation between the spectral features of the Be star and the hot model spectrum, so that the CCF appears as a composite of a broad component from the Be star and a generally narrow component from the sdO star. We need to remove the Be star component from the CCF in order to isolate the part of CCF due to the sdO spectral features. The first step in this process is to register the Be component in velocity space, and in this section we describe how the radial velocities of the Be stars were measured.

The radial velocities of the Be stars were determined by forming the CCF of the observed spectrum with a model for the Be star itself. The Be star model spectrum was constructed from the TLUSTY BSTAR2006 grid (Lanz & Hubeny 2007) by interpolation in solar abundance model spectra for the effective temperature (T_{eff}) and surface gravity ($\log g$) given in Table 1. The interpolated spectrum was convolved with a rotational broadening function for the projected rotational velocity ($V \sin i$) from Table 1 and an interpolated, linear limb darkening coefficient from Kurucz LTE models derived by Wade & Rucinski (1985). The resulting CCFs are very broad (Fig. 2) and their central peaks may be influenced by correlation between

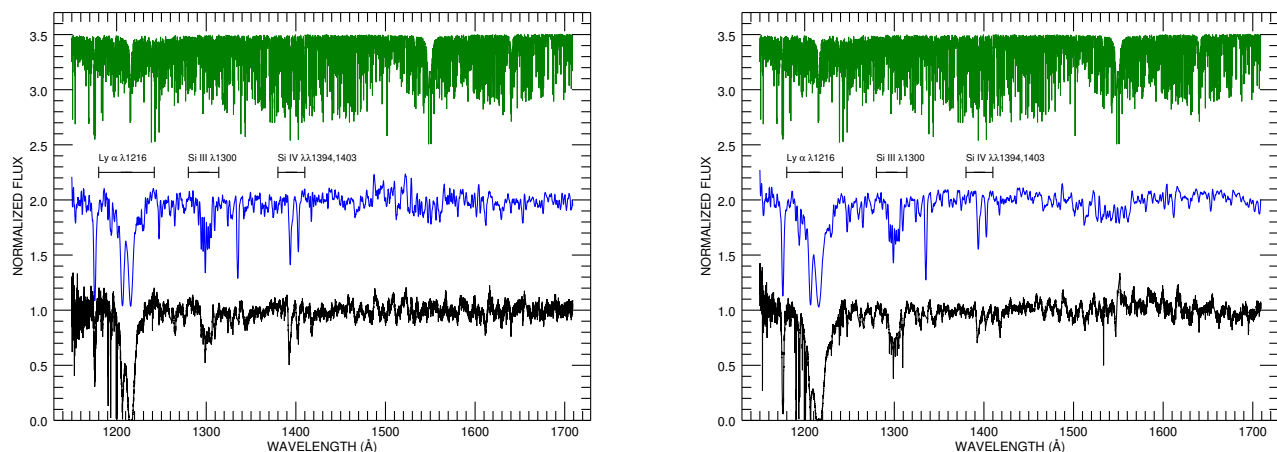


Figure 1. Left panel: HST/*STIS* spectrum of HD 43544 observed on HJD 2458707.4 (black). The TLUSTYB Be model spectrum is offset by +1.0 (blue) for parameters $T_{\text{eff}} = 21500$ K, $\log g = 3.9$, and $V \sin i = 260$ km s $^{-1}$ adopted from [Levenhagen & Leister \(2006\)](#). The TLUSTY model spectrum of the sdO component is offset by +2.5 (green) for $T_{\text{eff}} = 45000$ K. Right panel: HST/*STIS* spectrum of HD 55606 observed on HJD 2458756.7. The model spectra are plotted in the same format as HD 43544, except adopting parameters of the Be component, $T_{\text{eff}} = 27350$ K, $\log g = 4.3$, and $V \sin i = 335$ km s $^{-1}$, adopted from [Zorec et al. \(2016\)](#).

the Be model and the the central CCF peak from the sdO star. Consequently, we measured the Be star velocity by finding the wing bisector position using the Gaussian sampling method described by [Shafter et al. \(1986\)](#). The radial velocity uncertainties were calculated using the maximum likelihood from [Zucker \(2003\)](#), which is associated with the second derivative of the CCF peak, number of wavelength points within the CCF peak, and the peak height. Tests show that these errors are comparable to those obtained by selecting bisectors above and below the default value of 50% peak height. We report our radial velocity measurements and their uncertainties in columns 3 and 4, respectively, of Table 2.

4. DETECTION OF sdO COMPANION STARS

In order to confirm the detection of the hot subdwarf companions in these candidate sys-

tems, we adopted the methodology described in [Wang et al. \(2018\)](#) to search for the spectral signature of the subdwarf O-type (sdO) star by forming cross-correlation functions (CCFs) of the observed FUV spectra with a model spectrum for a very hot star. The default model spectrum was derived from the OSTAR2003 grid of solar abundance models based upon the non-local thermal equilibrium (non-LTE) atmospheres code TLUSTY and the associated radiative transfer code SYNSPEC ([Lanz & Hubeny 2003](#)). The adopted parameters for the model spectrum are $T_{\text{eff}} = 45$ kK, $\log g = 4.75$, and $V \sin i = 0$ km s $^{-1}$, and these are typical of estimates derived for known Be+sdO systems ([Wang et al. 2017](#)). The adopted gravity parameter is the highest value available in the OSTAR2003 grid, but it may underestimate the actual value for the subdwarf companions.

The CCFs should ideally reflect the photospheric absorption lines of the components, so

Table 2. Radial Velocity Measurements of Be+sdO systems

HD Number	Date (HJD-2,400,000)	V_{Be} (km s ⁻¹)	σ_{Be} (km s ⁻¹)	V_{sdO} (km s ⁻¹)	σ_{sdO} (km s ⁻¹)
29441	58769.2148	-2.1	11.1	17.1	3.3
29441	58717.5000	5.3	11.1	31.9	2.9
29441	58741.0742	1.1	11.0	38.9	3.1
43544	58707.3750	25.8	8.7	-37.9	1.5
43544	58774.0469	0.9	8.4	77.9	1.5
43544	58788.0156	8.8	8.2	54.0	1.7
51354	58748.7578	48.2	10.6	-58.8	6.4
51354	58762.1953	36.5	10.6	-30.7	8.8
51354	58787.9570	56.5	11.3	42.6	6.4
55606	58756.6992	42.7	13.0	0.3	2.2
55606	58888.5820	32.5	12.7	20.4	2.3
55606	58899.5078	34.4	12.6	65.9	2.3
60855	58804.5664	59.1	6.9	32.9	2.5
60855	58810.5977	55.6	7.0	37.2	2.4
60855	58855.4219	53.6	7.0	52.9	2.3
113120	58768.0898	27.1	11.9	-2.2	1.9
113120	58783.7461	-6.1	12.3	30.8	1.9
113120	58885.8555	27.7	12.1	-30.0	1.6
137387	58781.8320	44.7	9.3	-17.4	2.1
137387	58787.8516	33.2	10.0	-0.5	2.0
137387	58880.1562	19.1	10.0	41.1	2.2
152478	58709.7188	27.7	9.1	41.0	2.3
152478	58715.5430	28.0	8.9	47.4	2.3
152478	58761.2891	27.8	9.4	58.3	2.2
157042	58731.9102	-0.7	7.2	41.5	3.0
157042	58750.6367	-11.1	7.3	-14.2	3.4
157042	58767.2422	2.1	7.3	-26.3	3.1
157832	58731.9766	27.4	7.3
157832	58750.7070	27.4	7.8
157832	58772.2148	19.8	7.8
191610	58718.1445	-26.1	8.7
191610	58726.9453	-23.1	8.2
191610	58753.7656	-23.5	7.7
194335	58718.2695	8.4	10.3	53.3	1.5
194335	58727.0117	-7.3	10.6	42.6	1.7
194335	58755.4883	4.0	8.8	-88.6	1.5
214168	58734.2344	-4.0	11.0
214168	58753.7070	1.9	10.9
214168	58772.3047	-2.7	11.2

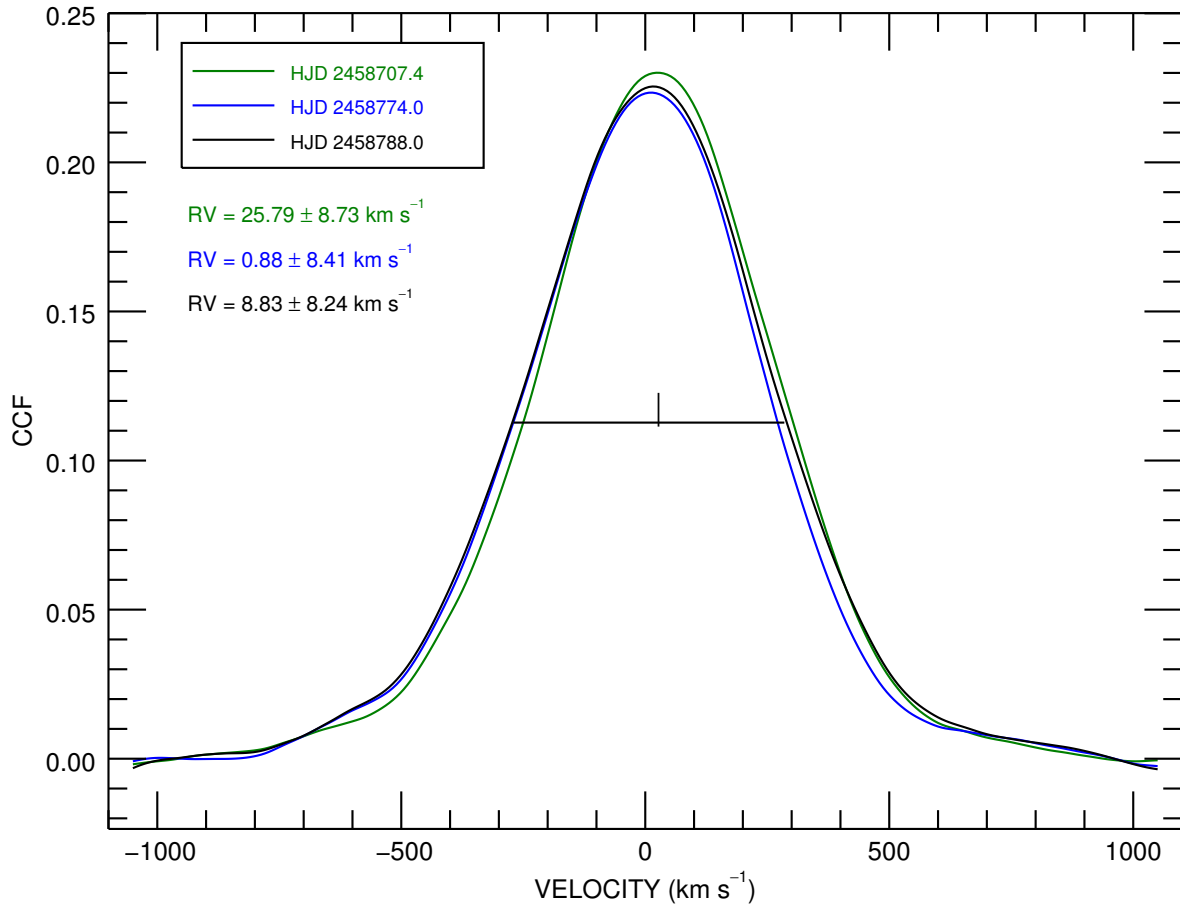


Figure 2. CCFs of observed FUV spectra of HD 43544 cross correlated with a TLUSTY BSTAR2006 Be model spectrum. Radial velocities were measured from the wings at 50% peak height of the CCFs by adopting the bisector technique as described in [Shafter et al. \(1986\)](#). The horizontal black line indicates the 50% peak height of the CCFs for the spectrum obtained on HJD 2458788.0, and the associated RV is shown as the tick mark.

we omitted those regions with spectral features that are much broader than the line profiles associated with rotational broadening. The omitted regions included the deep and broad absorption line profiles of Ly α λ 1216 and Si III λ 1300 blend, as well as the beginning and ending regions of the spectrum. In addition, we excluded the broad wind line features of Si IV $\lambda\lambda$ 1393, 1402 in the cases of HD 43544, HD 55606, HD 60855, HD 137387, HD 152478, and HD 194335. Both the Si IV $\lambda\lambda$ 1393, 1402 and C IV $\lambda\lambda$ 1548, 1550 wind lines were omitted in spectra of HD 29441, HD 113120, and HD 157042.

We caution that the solar abundance model spectrum used to represent the sdO spectrum may not match the abundance patterns accurately. Many low-mass sdO stars have spectra that are He rich with metallic line enhancements. For example, Rauch (1993) examined the FUV spectrum of the low-mass sdO star HD 128220 based upon 38 high resolution *IUE* spectra. Through a careful spectral analysis using non-LTE models, he found that the star has an effective temperature of $T_{\text{eff}} = 40.6 \pm 0.4$ kK, $\log g = 4.5 \pm 0.1$, and a mass of $0.54 \pm 0.01 M_{\odot}$. Furthermore, the star is helium rich with $n_{\text{He}}/n_{\text{H}} = 0.30 \pm 0.05$. Because this subdwarf star has measured T_{eff} and $\log g$ values that are similar to our model template, but with enhanced helium abundance, it provides a good test case of the applicability of our adopted solar abundance model. We downloaded from MAST¹ a high resolution SWP spectrum of HD 128220 made on HJD 2,444,256.0. The spectrum was reduced and rectified following the procedures reported in Wang et al. (2018). In Figure 3, the spectrum of HD 128220 is illustrated in black in the left panel, and the TLUSTY model spectrum of the subdwarf component is offset by +1.0 and shown in green. In

order to bring the observed spectrum into agreement with the rest frame of the model spectrum, we shifted the observed spectrum by adopting a radial velocity of $RV = 15.2 \pm 2.2$ km s⁻¹ from Howarth (1987) for the date of observations. We then cross correlated the observed spectrum with the TLUSTY model spectrum. The resulting CCF is shown in the right panel in Figure 3. A sharp peak is clearly seen indicating the detection of the subdwarf star in HD 128220 using the model spectrum. Therefore, we can safely assume that the TLUSTY model spectrum provides a sufficiently good match of an sdO spectrum for application in our search for their spectral signature in the observed *HST* spectra.

The resulting CCFs generally are very broad because of correlation of the model lines with the rotationally broadened lines of the Be star. In those cases of a positive detection, the CCF appears to show a sharp peak from the sdO spectral features that is superimposed on top of the broad CCF component from the Be star. We applied the following method to remove the Be component from the CCFs and isolate the signal from the sdO star. We first calculated a CCF for model spectra of both the Be star (using the parameters in Table 1) and the sdO star. This simulated CCF was shifted from the zero velocity frame to the specific radial velocity of the Be star from Section 3 (Table 2), and the CCF amplitude was rescaled to match that of the wings in the CCF of the observed spectrum with the model sdO spectrum. In many cases, we found that the CCF of the model Be and model sdO spectrum did not match well with the observed CCF width, so we reset the value of the projected rotational velocity $V \sin i$ for the model Be star spectrum in order to attain a better fit of the CCF wings. These adjusted $V \sin i$ values are listed in the final column of Table 1, and the uncertainties are of order 10% because the widths were set by visual inspection. Once the simulated Be model plus sdO

¹ <https://archive.stsci.edu/iue/>

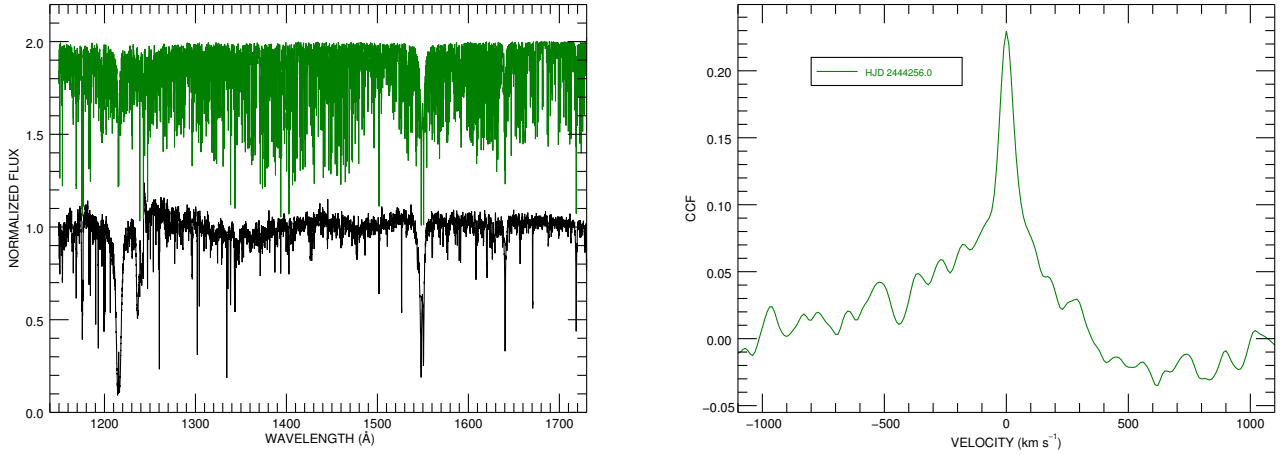


Figure 3. Left panel: The *IUE/SWP* spectrum of HD 128220 (black) made on HJD 2444256.0. The TLUSTY model spectrum of the sdO component is offset by +1.0 (green) for $T_{\text{eff}} = 45$ kK. Right panel: The CCF of the observed spectrum of HD 128220 cross correlated with the TLUSTY sdO model spectrum.

model CCF was registered in velocity, adjusted in width, and rescaled in CCF amplitude, we then subtracted this model from the CCF of the observed spectrum and model sdO spectrum. This procedure is illustrated in Figure 4 for the case of one observation of HD 137837. We see that the simulated CCF from the model Be star and model sdO star spectrum does match the observed CCF wings, and by subtracting this component, we form a residual CCF that clearly shows the narrow central peak from correlation with the sdO spectral lines alone.

We examined the residual peaks formed this way for all the observed spectra, and we detected CCF peaks from a hot subdwarf companion in ten Be+sdO targets. These positive detections were re-analysed using a grid of test effective temperatures for the sdO component (see Section 5), and we adopted the temperature that maximized the residual CCF peaks as the default for the model sdO spectrum. We then repeated the procedure of subtracting the Be component in the CCF using a model with the adopted sdO temperature instead of the default

$T_{\text{eff}} = 45$ kK value. The final residual CCFs are plotted for the ten positive detection cases in Figures 5, 6, and 7. No residual peaks were found that were significantly larger than the variation in the CCFs far from zero velocity for HD 157832, HD 191610, and HD 214168. The residual CCFs for these three non-detections are shown in Figure 8 and are based on the default $T_{\text{eff}} = 45$ kK model for an sdO component. It is puzzling that no obvious CCF peaks were found for these three cases, given that clear peaks were detected in CCFs constructed in a similar way for the lower S/N *IUE* spectra (and often in multiple observations) (Wang et al. 2018). This may result from temporal variations in the overall visibility of the spectral lines of the sdO component (Section 8).

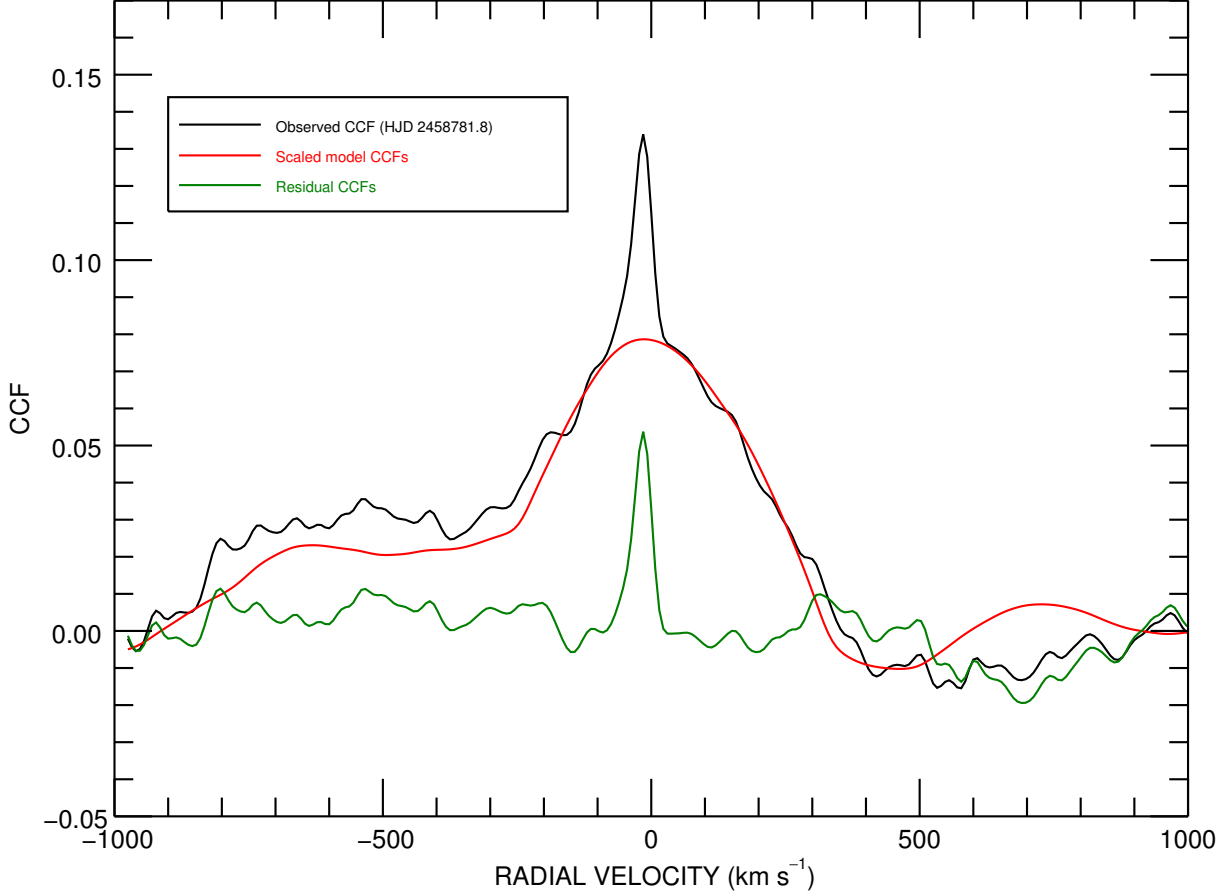


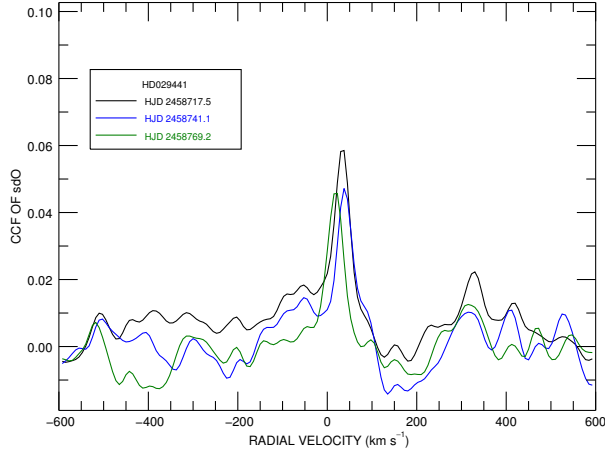
Figure 4. The CCF of the observed spectrum of HD 137387 observed on HJD 2458781.8 from cross correlation with the TLUSTY model spectrum. A scaled Be model spectrum (red) was subtracted from the composite feature, and the corresponding residual CCF (green) is associated with the sdO companion.

5. PHYSICAL PROPERTIES OF THE sdO STARS

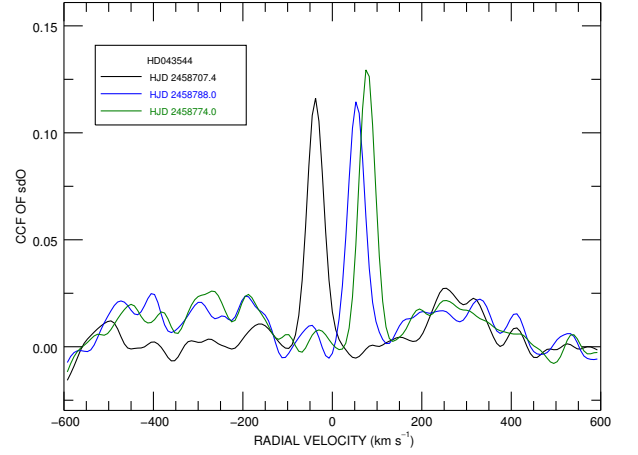
5.1. Radial Velocities

Inspection of the residual CCFs formed by subtracting the Be star component shows the presence of narrow peaks that are associated with the sdO spectral lines (Figs. 5, 6, 7). We find that the peaks show distinct changes in Doppler shift that reflect the orbital motion of the sdO component. Most of the residual peaks are narrow with a broadening dominated by the instrumental profile and intrinsic line widths in

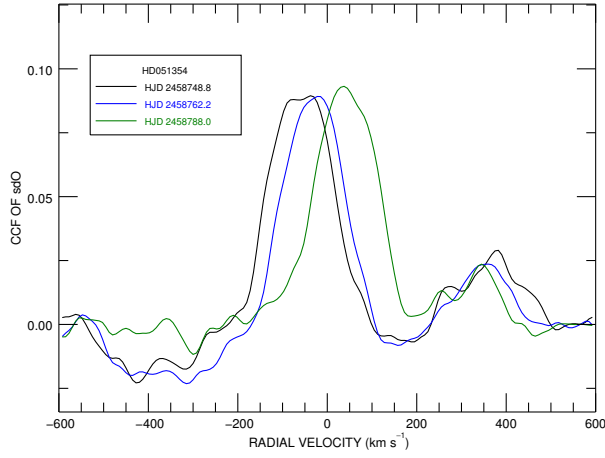
the CCF (Section 5.2). Consequently, we made simple Gaussian fits of the residual peaks in order to determine the Gaussian central position and its uncertainty. These radial velocities and their uncertainties are presented in columns 5 and 6, respectively, of Table 2 for the ten systems with positive detections. These velocity measurements will be valuable for future work on the determination of the orbital elements. Note that in principle it is possible to estimate the mass ratio from the co-variations of the Be star and sdO star radial velocities, but we found



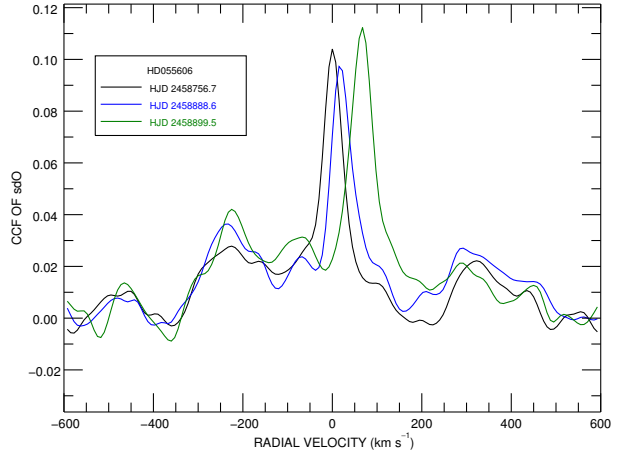
(a) HD 29441



(b) HD 43544



(c) HD 51354



(d) HD 55606

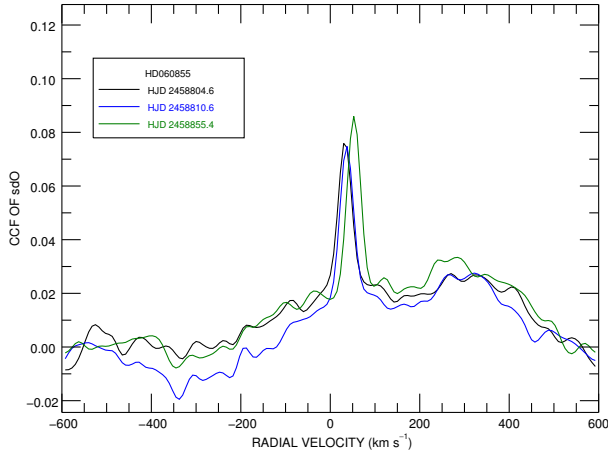
Figure 5. Residual CCFs of sdO companion stars in confirmed Be+sdO binary systems.

that the uncertainties in the Be star velocities were too large to establish any reliable limits on the mass ratio.

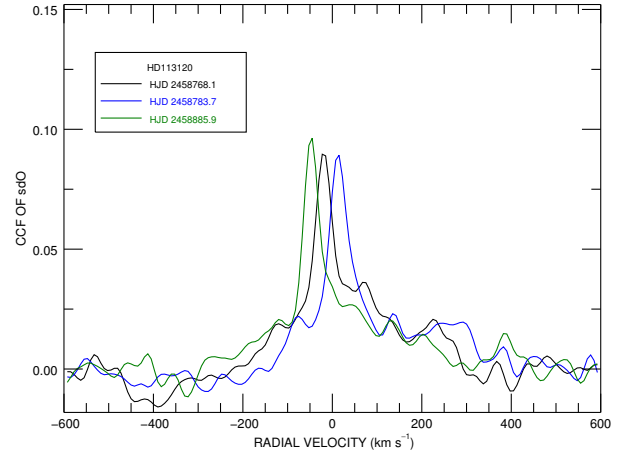
5.2. Projected Rotational Velocity

The width of the peak in the residual CCF is directly related to the projected rotational velocity $V \sin i$ of the sdO line profiles. We made a simulation of the dependence of the CCF peak FWHM (from Gaussian fits) as a function of assumed $V \sin i$ by calculating model spectra on

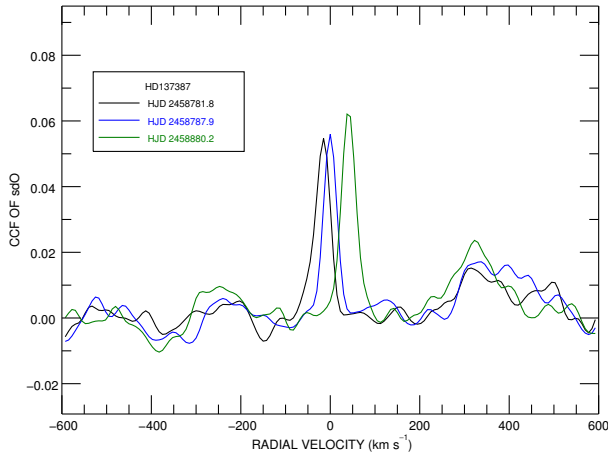
the observed grid that were convolved with a rotational broadening function for a range in $V \sin i$. We then formed CCFs of these model spectra with the adopted model sdO spectrum, and we made Gaussian fits of the resulting CCF peaks to build a functional relation between $V \sin i$ and CCF FWHM. An example of this relation from the numerical tests is shown in Figure 9. Comparison of the observed FWHM results with these relations indicates that the



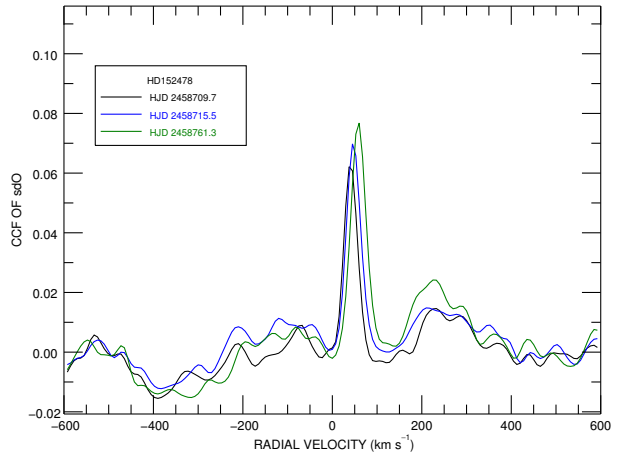
(a) HD 60855



(b) HD 113120



(c) HD 137387



(d) HD 152478

Figure 6. Residual CCFs of sdO companion stars in confirmed Be+sdO binary systems.

sdO star spectral lines are mainly unresolved in the $R = 20000$ versions of *HST*/STIS spectra. The only exception is the case of HD 51354 that shows significantly broader CCF peaks than those in any of the other detected sdO targets. The derived value of $V \sin i$ for HD 51354 is given in column 3 of Table 3, and upper limits are reported for the other nine cases where the sdO signal is detected. The uncertainty in $V \sin i$ is the standard deviation of the derived

values from the FWHM measurements in the residual CCFs of the three observations. The upper limits are set by the largest estimate from the three spectra or by the limit associated with the spectral resolution.

5.3. *Effective Temperature*

The residual CCF peak heights are sensitive to the degree of agreement between the model sdO spectrum and the sdO line contribution to the observed spectrum. The model properties

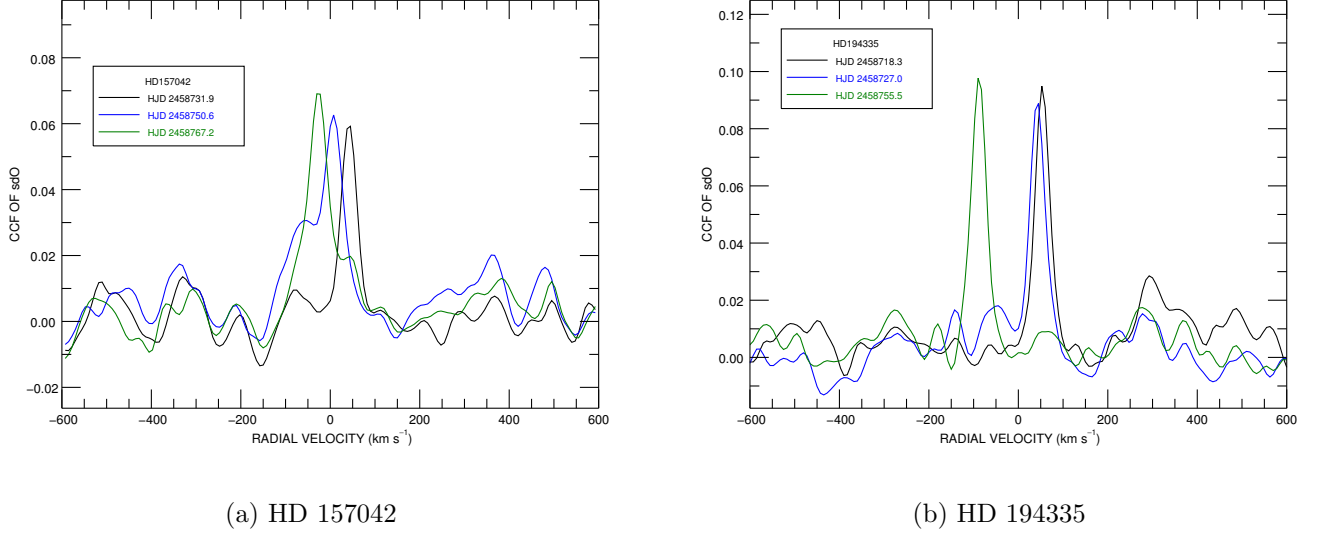
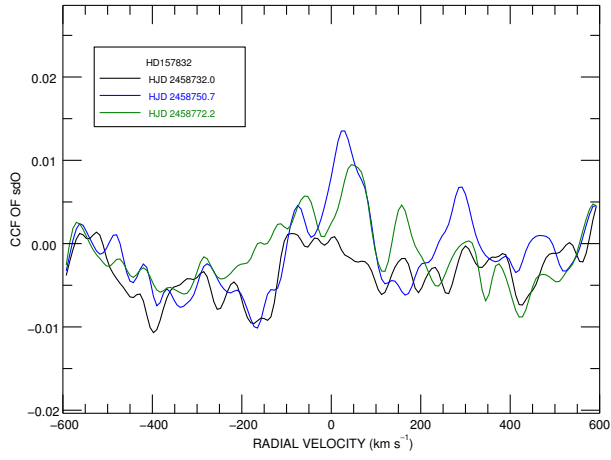


Figure 7. Residual CCFs of sdO companion stars in confirmed Be+sdO binary systems.

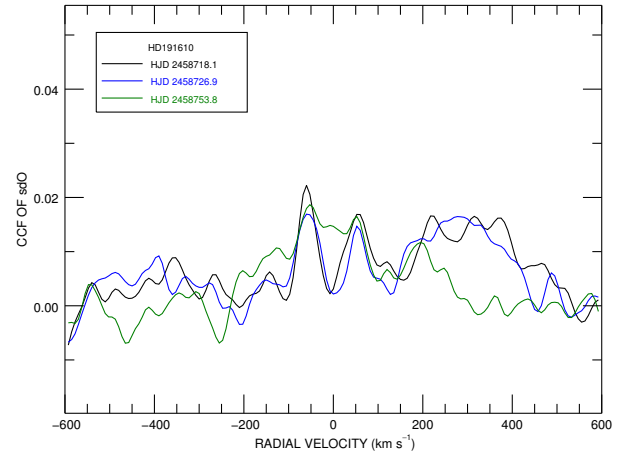
Table 3. Physical properties of sdO stars

HD Number	T_{eff} (K)	$V \sin i$ (km s $^{-1}$)	f_2/f_1	F_2/F_1	R_2 (R_{\odot})	$\log L$ (L_{\odot})
29441	40000	< 15	0.027 ± 0.003	9.9 ± 2.4	0.28 ± 0.04	$2.26^{+0.14}_{-0.21}$
43544	38200	< 15	0.090 ± 0.009	6.8 ± 1.5	0.51 ± 0.08	$2.70^{+0.15}_{-0.23}$
51354	43500	102 ± 4	0.099 ± 0.027	11.7 ± 2.7	0.47 ± 0.09	$2.85^{+0.13}_{-0.18}$
55606	40900	< 24	0.041 ± 0.002	8.4 ± 1.9	0.31 ± 0.04	$2.38^{+0.13}_{-0.19}$
60855	42000	< 27	0.041 ± 0.003	10.9 ± 2.6	0.50 ± 0.07	$2.85^{+0.14}_{-0.20}$
113120	45000	< 36	0.041 ± 0.009	7.6 ± 3.6	0.30 ± 0.10	$2.52^{+0.23}_{-0.53}$
137387	40000	< 17	0.032 ± 0.003	4.8 ± 1.0	0.44 ± 0.06	$2.65^{+0.14}_{-0.20}$
152478	42000	< 15	0.049 ± 0.003	11.5 ± 2.7	0.27 ± 0.04	$2.31^{+0.14}_{-0.21}$
157042	33800	< 36	0.026 ± 0.003	2.5 ± 0.6	0.61 ± 0.09	$2.64^{+0.15}_{-0.23}$
157832	45000 ^a	...	< 0.007	5.2	< 0.37	< 2.70
191610	45000 ^a	...	< 0.024	11.5	< 0.19	< 2.13
194335	43500	< 15	0.047 ± 0.007	4.8 ± 0.9	0.52 ± 0.07	$2.94^{+0.15}_{-0.23}$
214168	45000 ^a	...	< 0.019	3.6	< 0.42	< 2.82

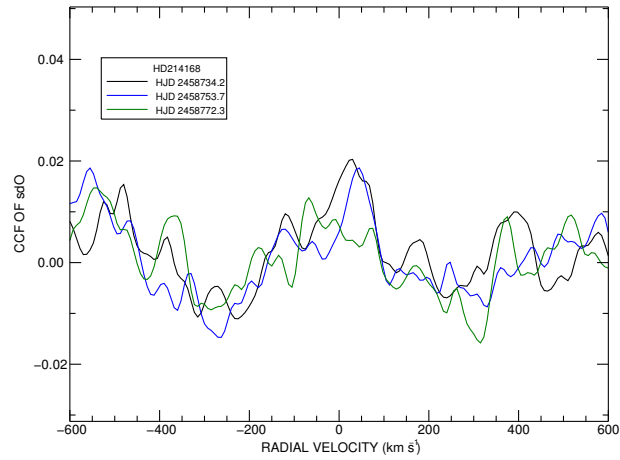
^aAssumed sdO temperature value.



(a) HD 157832



(b) HD 191610



(c) HD 214168

Figure 8. Residual CCF plots for the null detections.

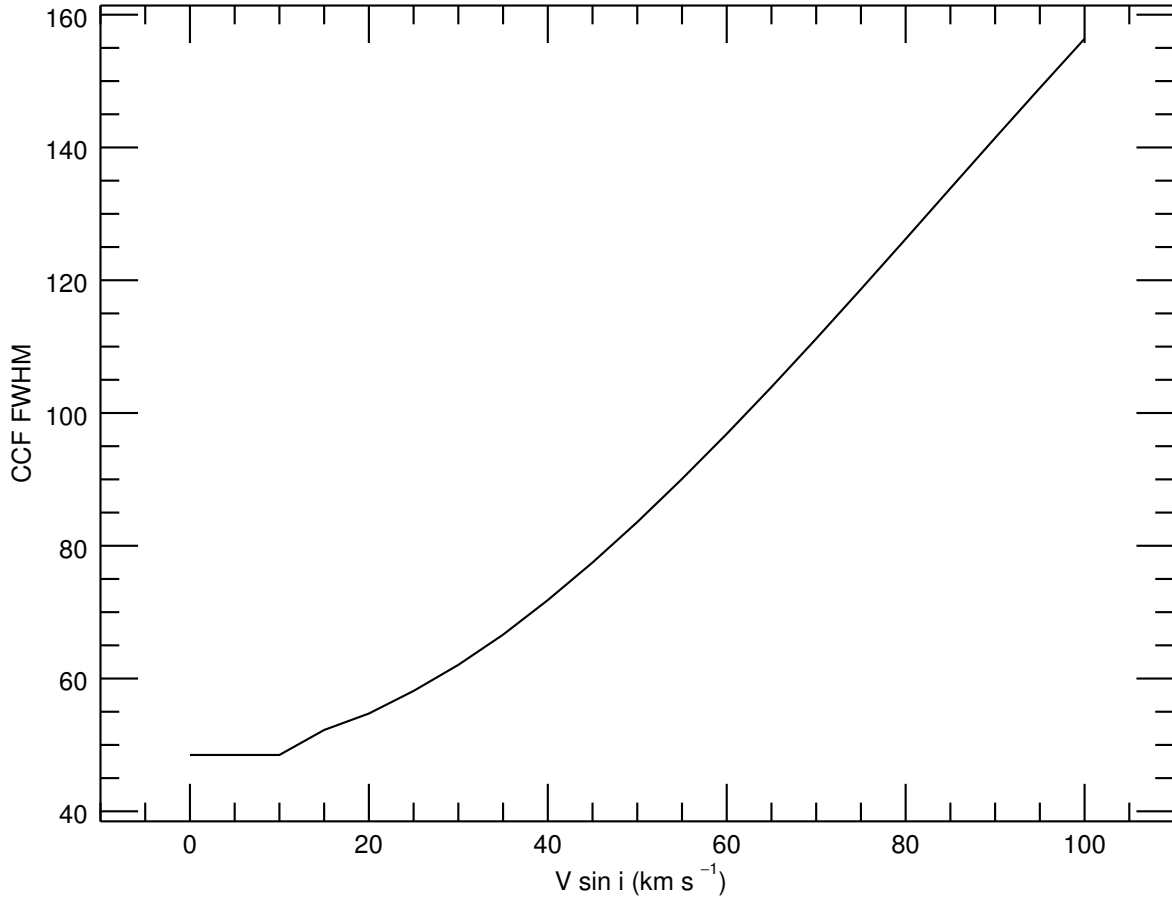


Figure 9. The distribution of CCF full width at half maximum (FWHM) as a function of assumed model sdO $V \sin i$ values in the binary system HD 43544. Note that no rotational broadening is applied in the models for $V \sin i \leq 10 \text{ km s}^{-1}$.

are primarily set by the assumed effective temperature, so for each positive detection, we calculated residual CCFs over a range in assumed sdO temperature in the same way as described above (Section 4) and then we measured the resulting peak height. Figure 10 shows the variation in peak height with assumed effective temperature T_{eff} for one observation of HD 43544 plus a spline fit of the relation. We took T_{eff} at the position of the maximum of the spline fit as the best estimate of temperature of the sdO star, and these are listed for the ten detected Be+sdO systems in column 2 of Ta-

ble 3. The range in the resulting T_{eff} values between observations is generally small, but given the uncertainty in the other model parameters (such as how much the actual gravity differs from the assumed $\log g = 4.75$), we estimate that temperature uncertainties are comparable to the grid step size in the OSTAR2003 models, $\Delta T_{\text{eff}} = 2.5 \text{ kK}$.

5.4. Monochromatic Flux Ratio

The height of the residual CCF peak is closely related to the flux contribution of the sdO star to the combined FUV flux. We relied upon a

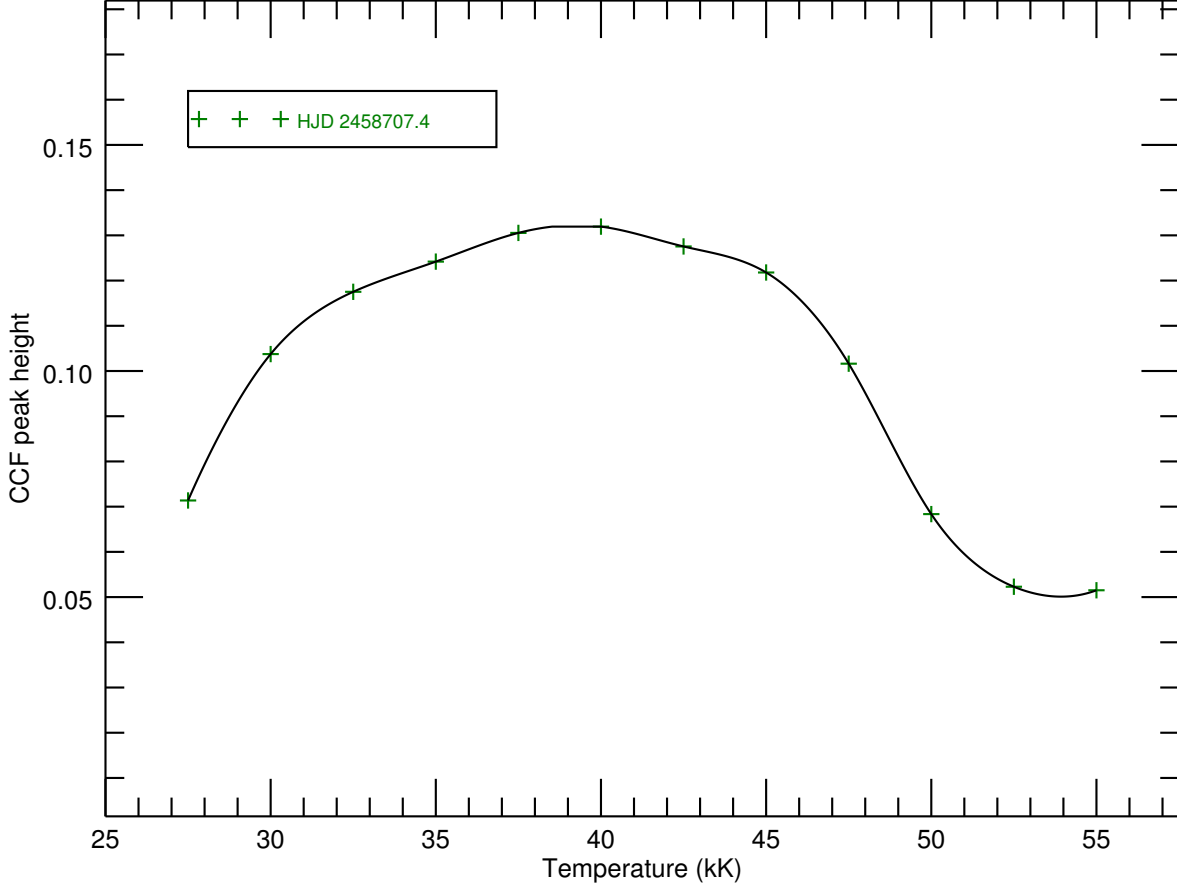


Figure 10. Distribution of CCF peak heights as a function of T_{eff} of the sdO companion in the binary system HD 43544 calculated for the spectrum obtained on HJD 2458707.4. A spline fit was applied to the distribution to estimate the effective temperature of the sdO companion from the value where CCF reaches a local maximum.

simulation of the residual CCFs for models of the spectra of the Be star and sdO star that were made over a range of test values of monochromatic flux ratio $r = (f_2/f_1)$. Each composite model was created using the best fit parameters for the Be star from Table 1 (from the BSTAR2006 grid) and for the sdO star from Table 3 (from the OSTAR2003 grid), and then the two rectified spectra were added by

$$f(\text{model}) = (f(\text{Be}) + rf(\text{sdO})) / (1 + r). \quad (1)$$

This approach assumes a constant flux ratio across the observed wavelength range, which is a reasonable assumption given the high temperatures of both components. We then calculated the CCF of the model spectrum with an sdO model for the best fit T_{eff} and $V \sin i = 0 \text{ km s}^{-1}$ in the same way as we did for the observed spectra (Section 4). The Be contribution to the resulting CCF was then removed as done previously, and the residual CCF peak height for the sdO component was measured. The result is a relation between assumed flux ratio r and resid-

ual CCF peak height, and an example is shown in Figure 11. We interpolated within each of these target specific curves to determine the flux ratio r from the measured residual CCF peak heights. These flux ratio estimates and their standard deviations are listed in column 4 of Table 3.

The observed flux ratio f_2/f_1 is related to surface flux ratios F_2/F_1 and area ratio $(R_2/R_1)^2$ by

$$\frac{f_2}{f_1} = \frac{F_2}{F_1} \left(\frac{R_2}{R_1} \right)^2. \quad (2)$$

The surface fluxes were taken as the average fluxes from the TLUSTY/SYNSPEC flux models over the range 1450 – 1460 Å, which corresponds to the near center part of the observed wavelength range. These fluxes depend mainly upon the adopted temperatures of the Be and sdO stars, and the surface flux ratio F_2/F_1 is given in column 5 of Table 3. The uncertainty in this ratio was determined by the errors in the effective temperatures (assumed as $\sigma(T_{\text{eff}}) = 2.5$ kK). Thus, we can use the observed flux ratio and surface flux ratio to arrive at the radius ratio. In Section 6 below, we derive estimates for the Be star radius R_1 from the spectral energy distribution and distance. Then, we solve for the sdO star radius R_2 from the radius ratio, and these radii are given in column 6 of Table 3. Finally, we estimate the luminosity of the sdO star in column 7 using

$$\log L/L_{\odot} = 4 \log T/T_{\odot} + 2 \log R/R_{\odot} \quad (3)$$

in which the nominal solar temperature is $T_{\odot} = 5772$ K (Prša et al. 2016).

6. SPECTRAL ENERGY DISTRIBUTIONS OF Be STARS

The radius of the sdO star can be found from the radius ratio (Section 5.4) and the radius of the Be star. In this section, we estimate the Be star radius by comparing the observed spectral energy distribution (SED) with models for

the composite Be+sdO system in order to determine the Be star angular diameter. We then use a distance estimate to find the Be star physical radius, which in turn leads to the sdO star radius (Table 3).

The angular diameter of the limb darkened disk θ (in units of radians) of a single star is found by the inverse-square law:

$$\frac{f_{\lambda}(\text{observed})}{F_{\lambda}(\text{emitted})} = (R_{\star}/d)^2 10^{-0.4A_{\lambda}} = \frac{1}{4}\theta^2 10^{-0.4A_{\lambda}} \quad (4)$$

where the ratio of the observed and emitted fluxes depends on the square of the ratio of stellar radius R_{\star} to distance d and the interstellar extinction A_{λ} . Here we create a model spectrum for the Be+sdO system F_{λ} that is scaled to the Be star flux, and then we fit this to the observed flux f_{λ} to find the angular diameter θ and reddening $E(B - V)$. We adopted an extinction curve law A_{λ} from Fitzpatrick (1999) that is a function of the reddening $E(B - V)$ and the ratio of total-to-selective extinction $R = A_V/E(B - V)$ (set at a value of 3.1).

Low resolution ($R = 500$) model spectra were formed from surface fluxes from BSTAR2006 for the Be star and from OSTAR2003 for the sdO star using the atmospheric parameters listed in Tables 1 and 3, respectively. Then the combined spectrum is given by $F_{\lambda}(\text{Be}) + F_{\lambda}(\text{sdO})(R_2/R_1)^2$, using the radius ratio determined in Section 5.4. In the cases of the sdO non-detections (HD 157832, HD 191610, HD 214168), only the Be star flux is included in the model.

The flux versions of the *HST*/STIS spectra were averaged and rebinned into nine wavelength segments (effective resolution of ≈ 14) to represent the flux in the FUV. We then extended the wavelength range into the NUV by adding fluxes measured by the TD-1 mission (Thompson et al. 1978) and fluxes derived from the Johnson *UBV* magnitudes (Mermil-

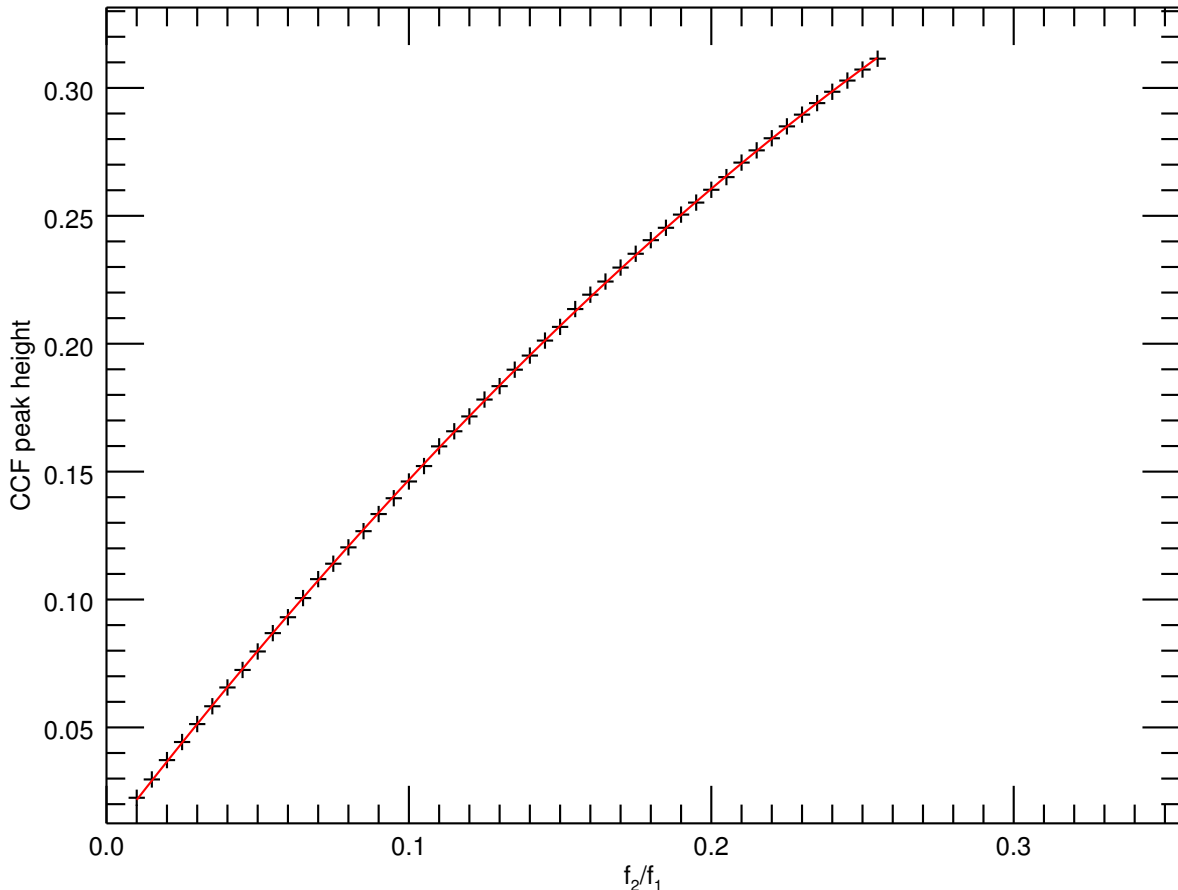


Figure 11. Distribution of the CCF peak heights as a function of assumed model flux ratio f_2/f_1 for the binary system HD 43544 calculated from TLUSTY model spectra. The final estimation of f_2/f_1 value of the sdO companion in the system was obtained through interpolating the observed CCF peak height to the distribution.

liod 1987) using the flux calibration of Colina et al. (1996). Longer wavelength fluxes were omitted because the Be star disks become important flux contributors beyond the optical range. There were two exceptions to this general scheme. The target HD 113120 has a close visual companion that is excluded in the small aperture for the *HST*/STIS observations, but is present in the longer wavelength measurements, so the latter were corrected to correspond to the Be+sdO system alone (see Appendix). The other target with a close com-

panion is HD 214168, and the three *HST*/STIS spectra record different amounts of companion flux (see Appendix). In this case, we selected the spectrum with lowest flux as most representative of the Be star (no sdO detection) and then adjusted the longer wavelength fluxes for the Be star alone.

The composite model spectra were fit to the observed SED using the relation above and the non-linear, least-squares fitting code MPFIT (Markwardt 2009) to find the best-fit values of $E(B - V)$ and θ that are listed in columns 2

and 5 of Table 4, respectively. The observed and model fit SEDs are plotted in Figures 12, 13, and 14 for systems with sdO detections (Be+sdO model fluxes) and in Figure 15 for the sdO non-detections (Be model fluxes only). The fluxes increase towards the shorter FUV wavelengths because of the hot temperatures of the targets and their companions, and the extinction and reddening values are relatively small in all cases. Column 3 of Table 4 lists published estimates of $E(B-V)$ from references cited in column 4. These published values agree with our measurements within 0.1 mag. We include in column 6 of Table 4 the Be star angular size estimates from the JMMC Stellar Diameters Catalog (Bourgés et al. 2014) for comparison with our result θ . In most cases there is satisfactory agreement, but we caution that the JMMC results do not account for the flux of the sdO and other companions.

We multiply the angular sizes by the distance to arrive at the physical radii of the Be stars. The distances from the Gaia DR2 survey (Bailer-Jones et al. 2018) are given in column 5 of Table 4, with the exception of the case of HD 113120 where the *Hipparcos* distance is adopted (see Appendix). The Be star radii appear in the final column of Table 4, and they are close to expectations for B-type main sequence stars (except perhaps for HD 157832; see Appendix). We used these Be star radii estimates together with the ratio of the radii derived from the flux ratios to find the sdO star radii that are given in column 6 of Table 3 (Section 5.4).

7. EVOLUTIONARY TRACKS FOR THE SUBDWARF STARS

Götberg et al. (2018) explored the properties of the stripped stars in binaries by calculating MESA evolutionary tracks for the mass donor stars. These models assume a Case B scenario in which mass transfer occurs as the initially more massive star expands as it evolves towards the red giant phase. After losing the outer

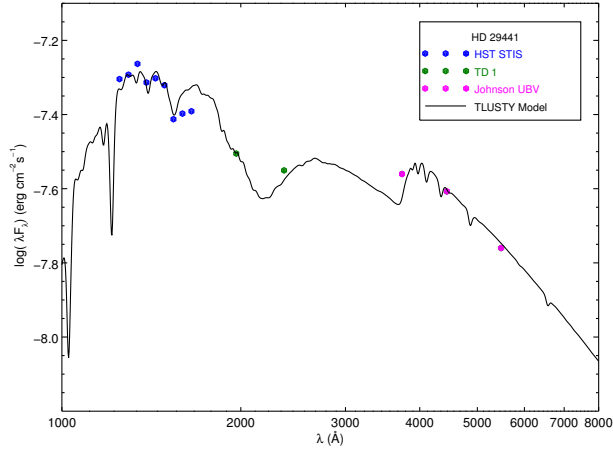
envelope, the remnant spends about 10% \sim 20% of its lifetime as a He-core burning, hot subdwarf. We show examples of the evolutionary tracks from Götberg et al. (2018) in $(\log T_{\text{eff}}, \log R/R_{\odot})$ and $(\log T_{\text{eff}}, \log L/L_{\odot})$ diagrams in Figures 16 and 17, respectively. These particular tracks assume an initial solar composition for the star. Four tracks are illustrated in each case for initial masses of 3.30, 3.65, 4.04, and 7.37 M_{\odot} for the mass donor star (sdO progenitor). In both diagrams, we see how the star evolves from the main sequence to cooler temperature and larger size. In the case of the low mass sdO progenitor (3.30 M_{\odot}), the star grows to fill its Roche limit after a period of 300 Myr. Once large scale Roche lobe overflow commences, the donor star is quickly transformed to a hotter and smaller (less luminous) object, a stage that may last only 3 Myr. The star then continues He-core burning for another 60 Myr in the portion of the tracks just beyond the first minimum in radius and luminosity (see also Fig. 2 in Götberg et al. 2018). The masses of sdO remnant at this stage are 0.67, 0.74, 0.85, and 1.85 M_{\odot} for the four mass tracks, respectively.

We include in Figures 16 and 17 our estimates for the sdO stellar parameters as summarized in Table 3. We also plot the parameters for the five Be+sdO systems that were known prior to our study. We see that most of the sdO companions do indeed have temperatures, radii, and luminosities that are comparable to the predictions from Götberg et al. (2018) for progenitors with masses in the range of 3 to 5 M_{\odot} . The sdO companions in four of our stars (HD 29441, HD 55606, HD 113120, and HD 152478) are shown at the He-core burning stage on the evolutionary track, and the rest of the sdO stars are at an inflated stage either from an early contraction phase or the later inflation phase at the He shell burning stage. If the masses of the sample Be stars are typical of those of single B-stars

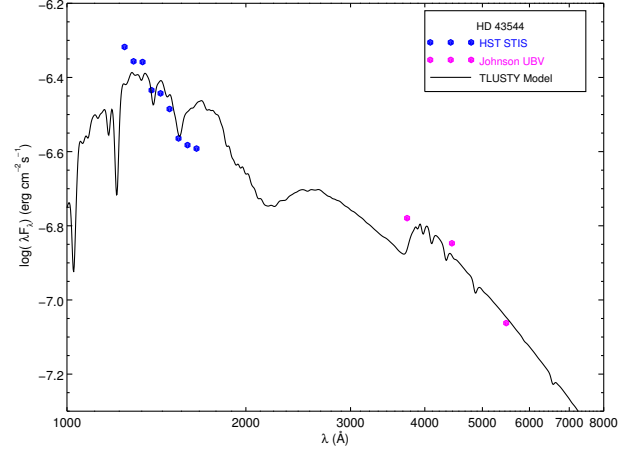
Table 4. Spectral energy distribution fitting parameters

HD	$E(B - V)_{HST}$ (mag)	$E(B - V)$ (mag)	Reference	θ (mas)	θ_{JMCC} (mas)	d (pc)	R_{Be} (R_{\odot})
29441	0.198 ± 0.014	0.202	1	0.0673 ± 0.0033	0.0763 ± 0.0030	737 ± 38	5.34 ± 0.38
43544	0.155 ± 0.024	0.054 ± 0.013	2	0.1315 ± 0.0113	0.1169 ± 0.0042	314 ± 6	4.44 ± 0.39
51354	0.172 ± 0.015	0.07	3	0.0779 ± 0.0042	0.0876 ± 0.0030	608 ± 21	5.09 ± 0.33
55606	0.220 ± 0.012	0.151 ± 0.100	2	0.0343 ± 0.0014	...	1090 ± 45	4.01 ± 0.23
60855	0.204 ± 0.016	0.295 ± 0.054	2	0.1586 ± 0.0092	0.1877 ± 0.0078	483 ± 25	8.24 ± 0.64
113120	0.176 ± 0.014	0.295 ± 0.054	2	0.1246 ± 0.0059	...	307 ± 57	4.11 ± 0.79
137387	0.125 ± 0.012	0.107 ± 0.009	2	0.1558 ± 0.0066	0.1599 ± 0.0060	326 ± 11	5.45 ± 0.29
152478	0.252 ± 0.011	0.241 ± 0.037	2	0.1274 ± 0.0051	0.1576 ± 0.0055	308 ± 7	4.21 ± 0.20
157042	0.187 ± 0.015	0.111 ± 0.027	2	0.1931 ± 0.0103	0.1845 ± 0.0164	291 ± 15	6.04 ± 0.44
157832	0.229 ± 0.011	0.138	1	0.1025 ± 0.0041	0.1341 ± 0.0052	1078 ± 85	11.88 ± 1.05
191610	0.182 ± 0.012	0.064 ± 0.019	2	0.2144 ± 0.0095	0.2140 ± 0.0079	188 ± 8	4.34 ± 0.27
194335	0.122 ± 0.017	0.045 ± 0.019	2	0.1311 ± 0.0078	0.1225 ± 0.0046	373 ± 11	5.26 ± 0.35
214168	0.025 ± 0.051	0.093 ± 0.024	2	0.0943 ± 0.0170	0.0899 ± 0.0035	590 ± 25	5.98 ± 1.11

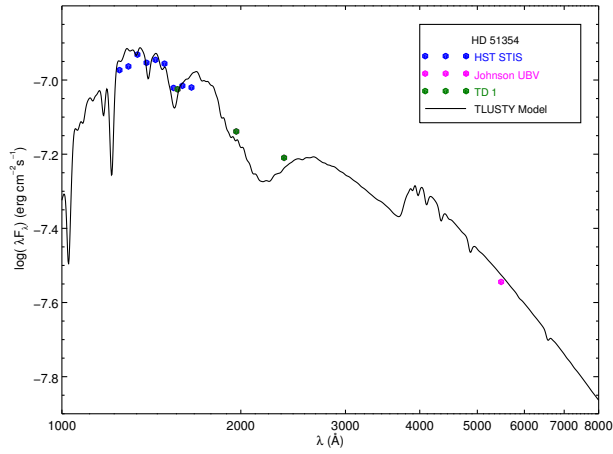
NOTE—Indices of references: (1) Kervella et al. (2019) (2) Zorec et al. (2016) (3) Gontcharov & Mosenkov (2018)



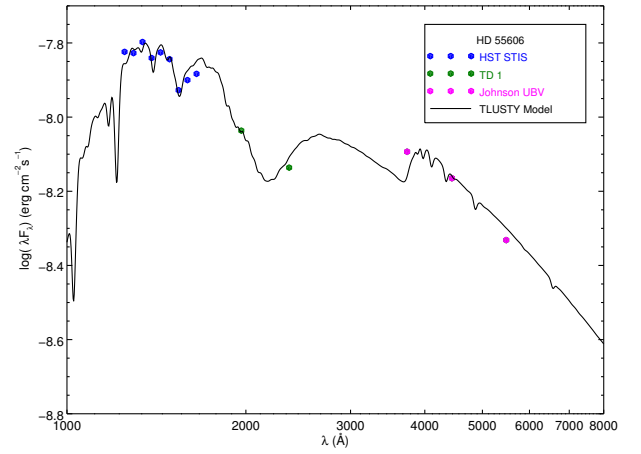
(a) HD 29441



(b) HD 43544

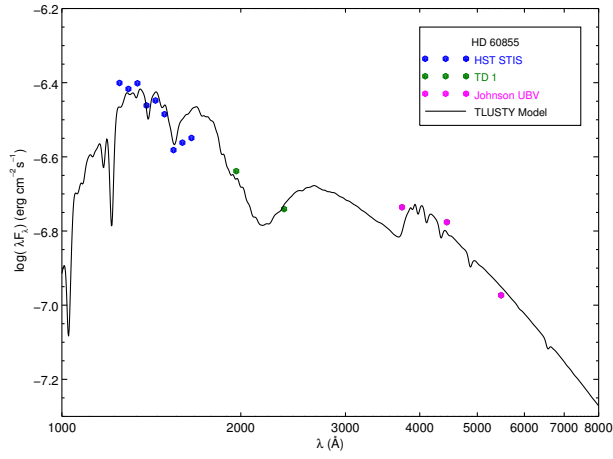


(c) HD 51354

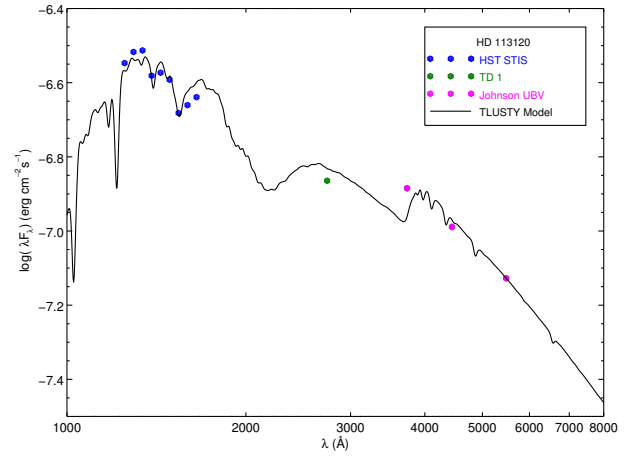


(d) HD 55606

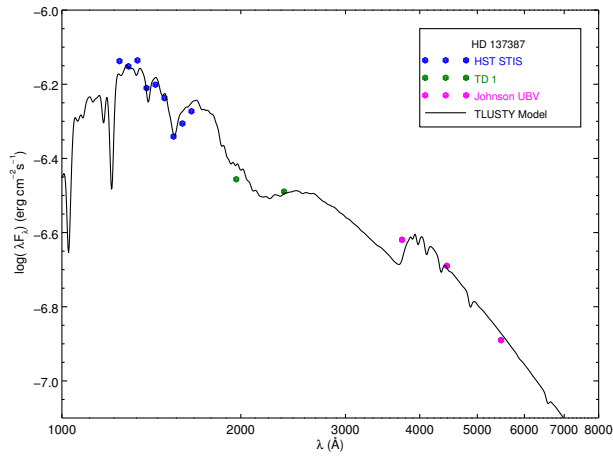
Figure 12. Spectral energy distribution of the Be stars: blue points are FUV *HST*/STIS observations, green points are UV observations from Thompson et al. (1978), and magenta points are optical Johnson *UBV* observations from Mermilliod (2006).



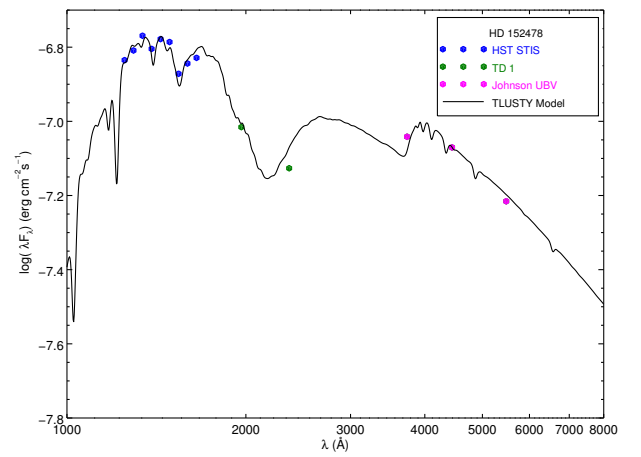
(a) HD 60855



(b) HD 113120



(c) HD 137387



(d) HD 152478

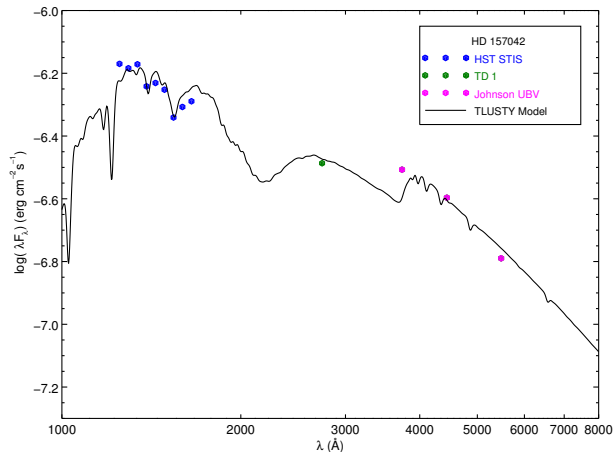
Figure 13. Spectral energy distribution of the Be stars in the same format as Fig. 12.

(≈ 4 to $8M_{\odot}$), then these systems probably began in near equal mass binaries, and systemic mass loss during the mass transfer phase was probably minimal.

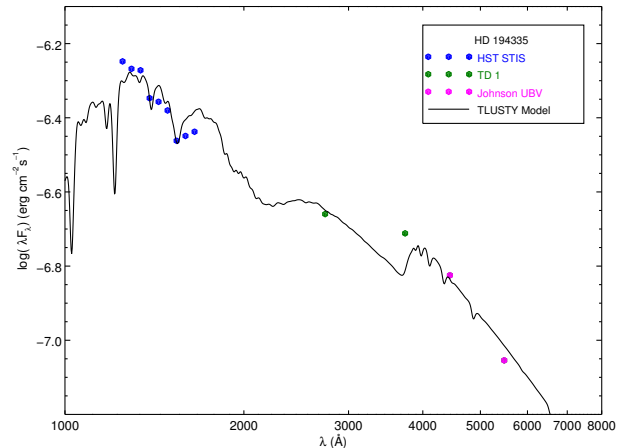
The only system in the sample with a known orbit and mass estimates is HD 55606, and Chojnowski et al. (2018) find a mass for the sdO star in the range 0.83 to $0.90M_{\odot}$. The evolutionary tracks suggest there is an approximately linear mass – luminosity relation during the He-core

burning stage (see Fig. 3 in Götzberg et al. 2018). Using the luminosity estimate for the sdO star in HD 55606 from Table 3, the tracks predict a mass in the range of 0.77 to $0.91M_{\odot}$, in agreement with observed estimate for the sdO star from Chojnowski et al. (2018).

Schootemeijer et al. (2018) created similar evolutionary tracks to study the current stage of the Be+sdO system ϕ Per. They concluded that the sdO star’s luminosity was large for its mass



(a) HD 157042



(b) HD 194335

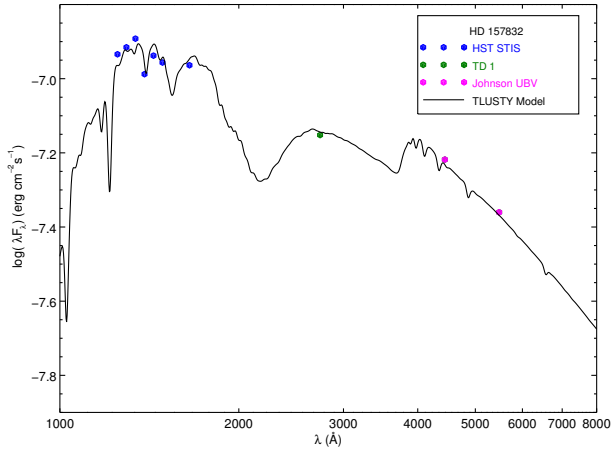
Figure 14. Spectral energy distribution of the Be stars in the same format as Fig. 12.

($1.2M_{\odot}$), and consequently the star may have entered the subsequent and short-lived He-shell burning stage of evolution. This also appears to be the conclusion from the tracks from [Götberg et al. \(2018\)](#) that show that the parameters of ϕ Per fall on a track for a more massive remnant ($1.85M_{\odot}$). [Schootemeijer et al. \(2018\)](#) argued that most of the Be+sdO binaries would have fainter sdO components found in the longer lasting He-core burning stage. The sdO companions discovered in the *HST*/STIS sample all have lower luminosities than that of ϕ Per, and this supports the idea that most such systems will be found in the fainter, He-core burning phase.

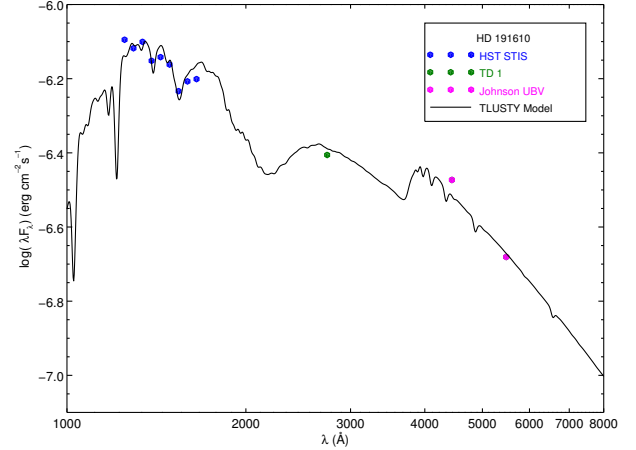
The faintest of the sdO companions plotted in Figures 16 and 17 is that in the HR 2142 system. [Peters et al. \(2016\)](#) described how the CCF peak strength from the sdO companion has an orbital phase dependence in the case of HR 2142, and they argued that the sdO star was obscured by varying amounts by circumstellar gas. Thus, the implied radius and luminosity of the sdO component in HR 2142 are both lower limits to the actual values.

8. CONCLUSIONS

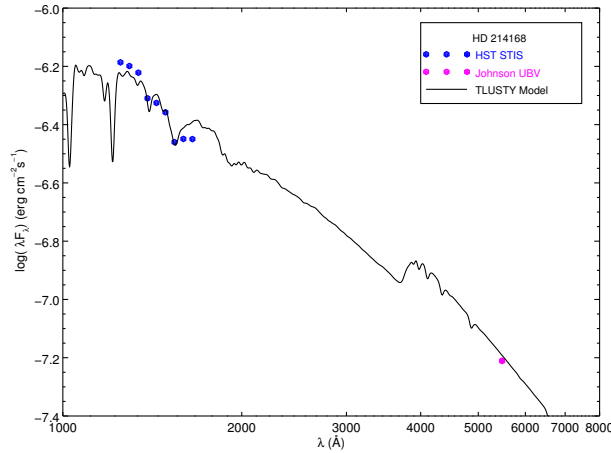
The primary goal of this investigation was to verify the presence of the spectral lines of hot subdwarf stars through a CCF analysis of FUV spectra from *HST*/STIS. We succeeded in detecting the CCF signal from the sdO star in nine of twelve candidates identified from lower quality *IUE* spectroscopy and in one case, HD 55606, where the sdO spectral features were first seen in optical spectra ([Chojnowski et al. 2018](#)). We can be confident that these detections are reliable, because the CCF peaks of the sdO component in these Be+sdO binaries are much narrower than the rotationally broadened component of the Be star, the peaks attain a maximum using a model CCF template for a star much hotter than the Be star, and the peaks display radial velocity variations indicative of Doppler shifts from orbital motion. On the other hand, the peak heights indicate that the sdO companions are relatively faint compared to their Be star primaries, which makes their detection difficult by other means. In fact, in our sample of 10 confirmed Be+sdO systems, only HD 55606 was known to be a binary prior to this work.



(a) HD 157832



(b) HD 191610



(c) HD 214168

Figure 15. Spectral energy distribution of the Be stars in the same format as Fig. 12.

The radial velocity measurements of the sdO components are an important first step in determining the orbital elements of the binaries and placing limits on the masses. The only system in the sample with a known orbit is HD 55606 with an orbital period of 93.76 days derived by Chojnowski et al. (2018), and the velocities from the *HST*/STIS spectra are consistent with their radial velocity curve for the sdO star. We combined the *HST*/STIS and *IUE* velocity

measurements to make a preliminary orbit for HD 194335 that indicates an orbital period of 60.3 days (see Appendix). We can make a rough estimate of the orbital period P of the other systems by assuming a probable Be star mass M_1 , system mass ratio $q = M_2/M_1$, and inclination i . For a circular orbit, the semiamplitude of the sdO star will be

$$K_2 = \frac{\sin i}{1+q} \frac{2\pi}{P} M_1^{1/3} (1+q)^{1/3} P^{2/3}. \quad (5)$$

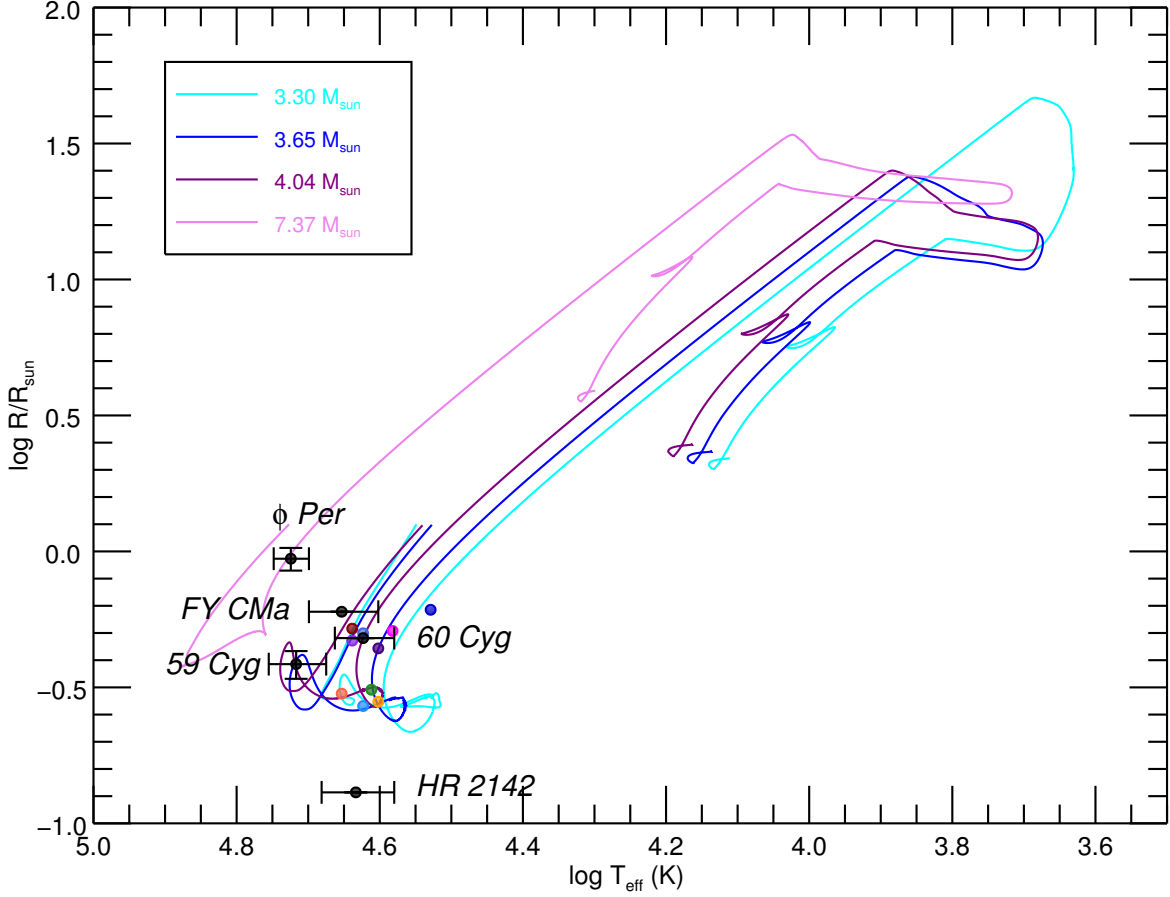


Figure 16. The evolutionary tracks in the $(\log T_{\text{eff}}, \log R_{\odot})$ plane of stripped stars with masses in a range of $3.30 - 7.37 M_{\odot}$ adopted from Götberg et al. (2018). The corresponding parameters of detected sdO stars are marked by filled circles and color coded as follows: HD 29441 (orange), HD 43544 (fuchsia), HD 51354 (blue violet), HD 55606 (forest green), HD 60855 (royal blue), HD 113120 (tomato), HD 137387 (indigo), HD 152478 (dodger blue), HD 157042 (medium blue), HD194335 (dark red). The five prior known Be+sdO binaries are shown in black circles.

If we assume $M_1 = 6M_{\odot}$, $q = 0.1$, and $i = 60^{\circ}$, then the predicted semiamplitude is $K_2 = 315 \text{ km s}^{-1} P^{-1/3}$, where the period is measured in days.

We can then make a numerical fit of the three observed radial velocities from *HST*/STIS by solving for three parameters: the period P , the epoch of maximum velocity T_0 , and the systemic velocity γ . The results range from $P = 84$ days for HD 137837 to $P = 346$ days for HD 60855.

These are nominally upper limits on the period because we make the simplifying assumption that the *HST*/STIS spectra cover only part of one orbit. Nevertheless, orbital periods on the order of months are what is found in the six other systems with known orbits and are consistent with the expectations for the enlargement of the orbit with mass transfer following mass ratio reversal (Wellstein et al. 2001).

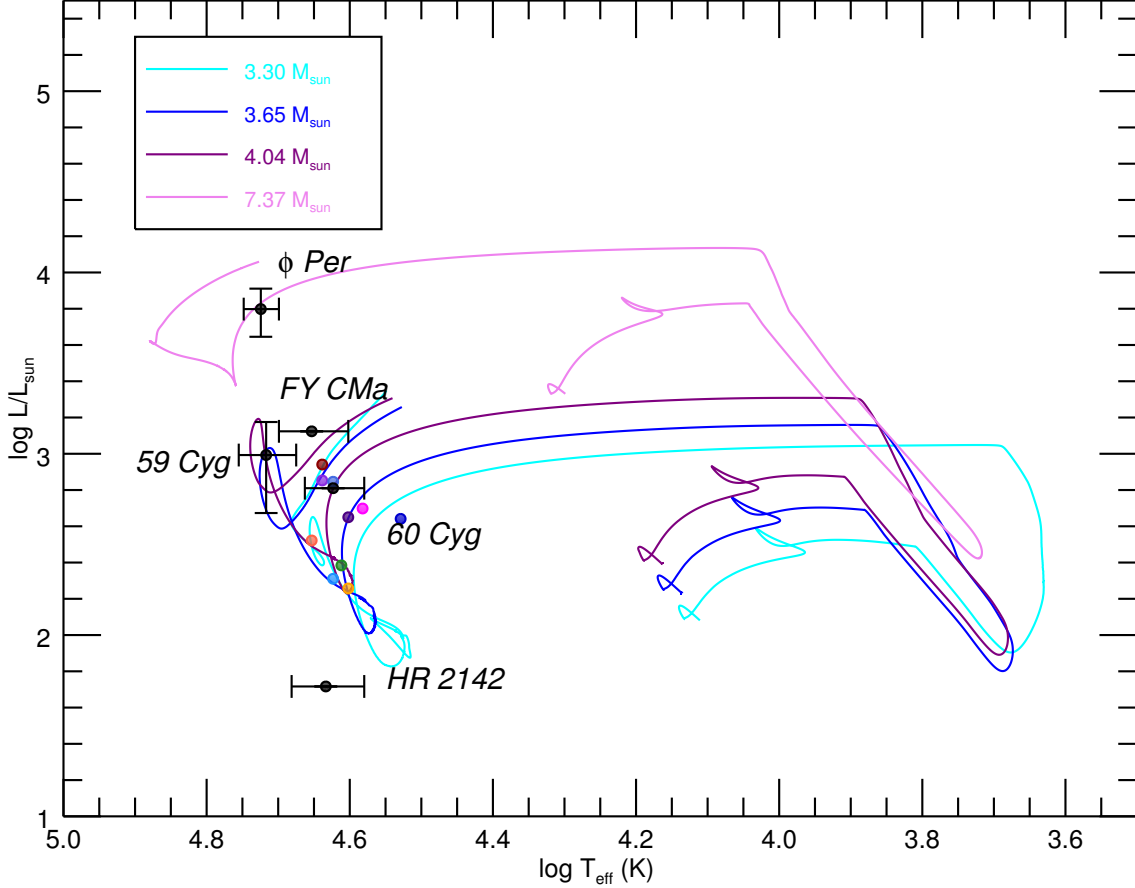


Figure 17. The evolutionary tracks in the $(\log T_{\text{eff}}, \log L_{\odot})$ plane of stripped stars with masses in a range of $3.3 - 7.37 M_{\odot}$ adopted from [Götberg et al. \(2018\)](#). The corresponding parameters of detected sdO stars are marked by filled circles and color coded as follows: HD 29441 (orange), HD 43544 (fuchsia), HD 51354 (blue violet), HD 55606 (forest green), HD 60855 (royal blue), HD 113120 (tomato), HD 137387 (indigo), HD 152478 (dodger blue), HD 157042 (medium blue), HD194335 (dark red). The five prior known Be+sdO binaries are shown in black circles.

The CCF peaks from the sdO components are generally narrow, and the derived projected rotational velocity $V \sin i$ is small (unresolved) except in the case of HD 51354 where $V \sin i = 102 \text{ km s}^{-1}$. We expect that the progenitors of the sdO stars attained synchronous rotation due to tidal forcing when they filled their Roche lobe, and consequently, their projected rotational velocities are small because of the long orbital periods and very small radii. The large $V \sin i$ of

HD 51354 may be the result of spin up by reverse mass transfer. The Be primary star loses mass into its outflowing equatorial disk, and some of this gas may end up being accreted by the sdO companion. The angular momentum carried by the accreted gas could lead to spin up. However, it is unknown why this process would occur in this Be+sdO system and not the others.

The peak heights of the sdO CCF component vary with the assumed temperature of the model spectrum used to form the cross-correlation function. We adopt a temperature that maximizes the CCF peak strength, and this yields effective temperatures in the range of 34 to 45 kK (Table 3). These are all much hotter than those of the Be stars and are close to model expectations for stripped stars (Section 7).

The CCF peak height also depends on the fractional flux contribution of the sdO spectrum to the total combined flux, and we used numerical simulations of model spectra for the Be and sdO stars to derive the monochromatic flux ratio in each case (Table 3). We can then compare the observed flux ratio with the surface flux ratio from the estimated temperatures of the components to find the radius ratio. We then determined the Be star radius from a fit of the spectral energy distribution and the distance (Section 6) to finally arrive at estimates of the sdO stellar radii (Table 3). Although the sdO stars contribute a minor fraction of the overall flux, it should be possible to find evidence of their spectral lines in high S/N optical spectra and to determine visual orbits for the closer systems through long baseline optical interferometry (Mourard et al. 2015).

The question remains about why we did not detect any clear sdO CCF peak in the *HST*/STIS spectra of HD 157832, HD 191610, and HD 214168, even though such peaks were detected in CCFs from lower quality *IUE* spectra (Wang et al. 2018). We note that in the latter two cases, there are many archival *IUE* spectra, but Wang et al. (2018) were only able to find significant CCF peaks for about half of those spectra (see Appendix). This suggests that there is an inherent temporal variability in the contribution of the sdO component to the combined FUV spectrum. A similar situation was found by Peters et al. (2016) for the Be+sdO system HR 2142, in which the detec-

tion of the peak was limited to certain parts of the orbit. We suspect that this variability is due changes in obscuration of the sdO star by nearby circumstellar gas. Thus, the non-detection of the sdO CCF peaks in these three cases does not necessarily imply that these are single Be stars that lack sdO companions.

We found that the derived temperatures and radii of the sdO components are broadly consistent with model predictions for stars stripped of their envelopes by binary interaction (Götberg et al. 2018). These parameters agree with the long-lived stage of He-core burning in the remnants that lasts about 10% \sim 20% of the star’s lifetime. There is a predicted relation between mass and luminosity at this stage, and our derived luminosity for the sdO in HD 55606 corresponds to a mass that agrees within uncertainties with that derived from the observations presented by Chojnowski et al. (2018).

The *HST*/STIS spectra of this sample of Be stars have given us a remarkable picture of how stars are transformed through binary interactions to create hot, stripped down subdwarfs. These spectra reveal the temperatures, radii, and hence, luminosities of the sdO stars, but what remains is to determine their masses by determining the full orbital elements. This is a difficult task because the sdO spectral lines in the optical part of the spectrum are weak and few in number, and the lines of the Be star are very shallow and broad ($V \sin i \approx 300 \text{ km s}^{-1}$) compared to the orbital semiamplitude ($K_1 < 10 \text{ km s}^{-1}$). Nevertheless, this observational work is essential in order to derive the component masses and to make detailed comparisons with model predictions (Götberg et al. 2018). Searches for Be+sdO systems among Be stars in clusters are particularly important to compare their ages to model predictions. The fact that Be stars lack main sequence companions compared to normal B stars is evidence that many Be stars are the descendants of pairs of inter-

acting binaries (Bodensteiner et al. 2020a), so there should be many examples of this hidden stage of evolution that remain to be discovered.

ACKNOWLEDGMENTS

We thank Denise Taylor of STScI for her help in planning the observations with *HST*. This work was supported by NASA through a grant from the Space Telescope Science Institute, under program GO-15659. Institutional support was provided from the GSU College of Arts and Science.

Facilities: HST (STIS), Gemini:Gillett (Alopeke)

APPENDIX

A. NOTES ON INDIVIDUAL STARS

HD 29441 (V1150 Tau). There is only one *IUE* high dispersion spectrum for this target, and the CCF peak of the hot component appears with a radial velocity of $V_r = -60.7 \pm 2.5 \text{ km s}^{-1}$ (Wang et al. 2018), compared to the positive radial velocities found here (Table 2). Slettebak et al. (1997) note that the star is distant from the Galactic plane, with $z = -308 \text{ pc}$ for the Gaia DR2 distance (Table 4). Slettebak et al. (1997) describe the broad lines in the optical spectrum, which they classify as B2 III/IVe.

HD 43544 (HR 2249). Levenhagen & Leister (2006) determined parameters for this star that they classify as B2/3 Ve, and they estimate an evolutionary mass of $8.5M_{\odot}$ for the Be star. The *HST*/STIS spectra CCF peaks show a large velocity range that spans the single *IUE* measurement (Wang et al. 2018). Huang et al. (2010) find a small velocity variation for the Be component between two observations.

HD 51354 (QY Gem). The CCFs of the hot companion are remarkably broad compared to all the other detections, and this was also found in the CCFs from two *IUE* spectra (Wang et al. 2018). These CCF peaks show large velocity variations, while velocity measurements of the Be star display relatively little scatter (Chojnowski et al. 2017).

HD 55606. The orbital variations of the hot, narrow-lined component were discovered in optical spectra by Chojnowski et al. (2018) who determined a double-lined orbital solution. The *HST*/STIS spectra CCF velocities are consistent with their orbit. There are no *IUE* observations for this target.

HD 60855 (HR 2921; V378 Pup). This star is a candidate blue straggler in the open cluster NGC 2422 (Pols et al. 1991), and it has several wide and faint companions listed in the Washington Double Star catalog. There are six *IUE* CCF velocity measurements, all of which are lower than the three measurements presented in Table 2.

HD 113120 (HR 4930; LS Mus). There are large velocity variations in both the three *IUE* (Wang et al. 2018) and *HST*/STIS spectra CCF measurements for the hot component. This star has a nearby companion at a separation of 0.56 arcsec (Hartkopf et al. 1996). It was also resolved by *Hipparcos* with a magnitude difference of $\Delta H_p = 2.84 \pm 0.04 \text{ mag}$ (ESA 1997). This companion falls outside the *HST*/STIS aperture, but its flux does contribute to the TD-1 and Johnson *UBV* measurements.

Consequently, we used ΔH_p to add 0.077 ± 0.003 mag to correct the TD-1 and *UBV* measurements (assuming similar colors for both components) to estimate the magnitudes and fluxes without the companion’s contribution. The SED fitting was made using these adjusted supplementary fluxes. The distance from Gaia DR2 is very uncertain (756 to 1496 pc; Bailer-Jones et al. 2018) probably due to complications from the companion’s flux. Krelowski et al. (2017) list three distance estimates: 250 pc from Ca II interstellar line strength, 307 pc from *Hipparcos* (van Leeuwen 2007), and 351 pc from spectrophotometric fits. We adopt the *Hipparcos* result in Table 4.

HD 137387 (κ^1 Aps; HR 5730). Boubert & Evans (2018) suggest that the object is a runaway star with a peculiar space velocity of 57 km s^{-1} , but Jilinski et al. (2010) derive a much lower value of 32 km s^{-1} . Jilinski et al. (2010) obtained seven radial velocities for the Be star and concluded that it is a binary. There are large velocity variations for the hot component in both the four *IUE* and three *HST/STIS* spectra CCF measurements.

HD 152478 (HR 6274; V846 Ara). There are two *IUE* velocity measurements with a large difference (Wang et al. 2018), while all three *HST/STIS* spectra CCF measurements are similar and redshifted. Jilinski et al. (2010) found that the Be star absorption lines are too broad ($V \sin i = 370 \text{ km s}^{-1}$) for reliable radial velocity measurements.

HD 157042 (ι Ara; HR 6451). This star displays relatively large velocity variations in both the four *IUE* and three *HST/STIS* spectra CCF measurements for the hot companion. The violet and red peaks of the H α emission show relative strength variations (Dachs et al. 1986, 1992; Mennickent & Vogt 1991) that may be related to orbital phase.

HD 157832 (V750 Ara). This candidate binary was identified by Wang et al. (2018) from CCF weak peaks observed in two *IUE* spectra. The residual peaks from the *HST/STIS* spectra CCFs are also weak (Fig. 7), which suggests that any hot component in this system is faint. The Gaia DR2 distance of 1078 pc (Bailer-Jones et al. 2018) may be too large. For example, Kozok (1985) gives a lower distance of 780 pc, and Lopes de Oliveira & Motch (2011) suggest an even smaller value of 530 pc. Thus, the Be star radius given in Table 4 may be an overestimate. Lopes de Oliveira & Motch (2011) discuss the hard and intense X-ray flux from this target, making this star an analog of the Be star X-ray emitter γ Cas. Langer et al. (2020) argue that such X-ray emission may originate where the wind from a hot sdO star strikes the outer region of the Be star disk.

HD 191610 (28 Cyg; V1624 Cyg). The CCF residuals shown in Figure 7 indicate little or no evidence of a hot component. Wang et al. (2018) examined 46 high dispersion SWP spectra from *IUE* to search for evidence of a CCF peak from a hot companion, and a peak was measured for only 25 of the 46 spectra (with CCF peak amplitude of ≈ 0.025). This suggests that there is some kind of temporal variability that makes detection more favorable at some epochs rather than others. Thus, we still regard HD 191610 as a viable Be+sdO candidate system, despite the non-detection in the *HST/STIS* CCFs. Becker et al. (2015) obtained 64 measurements of the Be star radial velocity from high signal-to-noise and high dispersion optical spectra, and they measured a residual “jitter” of 13.4 km s^{-1} , which is probably comparable to the orbital semiamplitude of the Be star.

HD 194335 (HR 7807; V2119 Cyg). The CCF peaks show large velocity variations in both the four *IUE* measurements (Wang et al. 2018) and in the three *HST/STIS* measurements (Table 2). We combined these to make a preliminary circular orbital fit with period $P = 60.286 \pm 0.010$ d, epoch of maximum velocity $T_0 = \text{HJD } 2,458,721.2 \pm 0.6$, systemic velocity $\gamma = -18.9 \pm 1.2 \text{ km s}^{-1}$, and

semiamplitude $K_1 = 75.5 \pm 2.4 \text{ km s}^{-1}$. The derived systemic velocity is comparable to the median from four measurements of the Be star, -30 km s^{-1} , made by Costado et al. (2017).

HD 214168 (8 Lac A; HR 8603). This star is a member of the Lac OB1 association (Kaltcheva 2009) and is the northern and brighter component of a pair separated by 22 arcsec. The target is also a close binary resolved by speckle interferometry (CHR 112 Aa,Ab; McAlister et al. 1987). Recently Tokovinin et al. (2019) presented an orbital solution based upon speckle measurements that yields an orbital period of 42 years and an angular semimajor axis of 0.057 arcsec. The derived total mass is $17 \pm 8 M_{\odot}$ based upon the distance from Gaia DR2 ($542 \pm 30 \text{ pc}$; Bailer-Jones et al. 2018). We obtained speckle observations with the Àlopeke instrument on the Gemini North Telescope on 2019 October 12 and with the 562 nm and 832 nm filters. The measured separation was 0.041 arcsec and position angle 133.4 degrees east from north, and this position is consistent with the orbit from Tokovinin et al. (2019). The average magnitude difference in the optical range from the Àlopeke and Tokovinin et al. measurements is $\Delta m = 0.43 \pm 0.10 \text{ mag}$.

The *HST*/STIS observations are centered on the brighter object within an aperture with a projected size of $0.2 \times 0.05 \text{ arcsec}$ on the sky, so some flux from the Ab component may be recorded in the spectra. We found that the measured flux in the 1300 - 1400 Å range was $(4.27, 4.72, 3.71) \times 10^{-10} \text{ erg cm}^{-2} \text{ s}^{-1} \text{ Å}^{-1}$ for the three observations consecutively, a much larger relative variation than observed in other targets, so we assume that the spectrum recorded more (less) flux from component Ab in the second (third) observation. However, there is no discernible difference between the three spectra, which suggests that the Ab component has a similar spectral appearance with broad lines and a temperature like that of the Be star.

We performed a CCF analysis to search for the spectral lines of the Ab component by constructing CCFs for a grid of lower temperature models and then removing the associated contribution to the CCF from the Be star in the same way as we did in the search for the signal of a hot companion. We detected a weak and narrow signal in the residual CCFs that is shown in Figure 18. The residual peaks attained maximum strength for CCF model spectra with $T_{\text{eff}} = 23 \pm 4 \text{ kK}$, and the width and height of the peak suggest $V \sin i = 31 \pm 5 \text{ km s}^{-1}$ and $f_2/f_1 \approx 0.07$, respectively. The measured velocities from Gaussian fits of the peaks are -31.6 ± 1.6 , -15.2 ± 1.8 , and $-24.1 \pm 1.3 \text{ km s}^{-1}$ for the three consecutive observations. We doubt that these peaks originate in the Ab component, because the flux ratio is much too small for the bright Ab component and because there is no evidence in published optical spectra for a narrow-lined spectral component as bright as Ab. It is unlikely that this CCF peak corresponds to a cooler, stripped companion, because the associated temperature of the feature is lower than that of the Be star, and in all the other cases, we find that the stripped down donor star is hotter than the bright mass gainer star. We also rule out an origin in interstellar lines, because we avoided these in forming the CCFs and the peaks appear to have a variable radial velocity. Instead, we suspect that this spectral signature is the result of line absorption from the disk of the Be star. Gies et al. (1998) found evidence of such absorption features in the Be+sdO system ϕ Per that appeared when the hot companion was in the foreground in the orbit. They surmised that these narrow “shell” absorption lines (mainly Fe IV) are formed as we view the Be star through heated portions of the outer disk. If the weak CCF signal shown in Figure 18 is related to shell absorption lines, then the like occurrence of these in the spectrum of ϕ Per suggests that HD 214168 may also have a close hot companion. However, there is no obvious signal from a hot companion in the CCF residuals (Fig. 8).

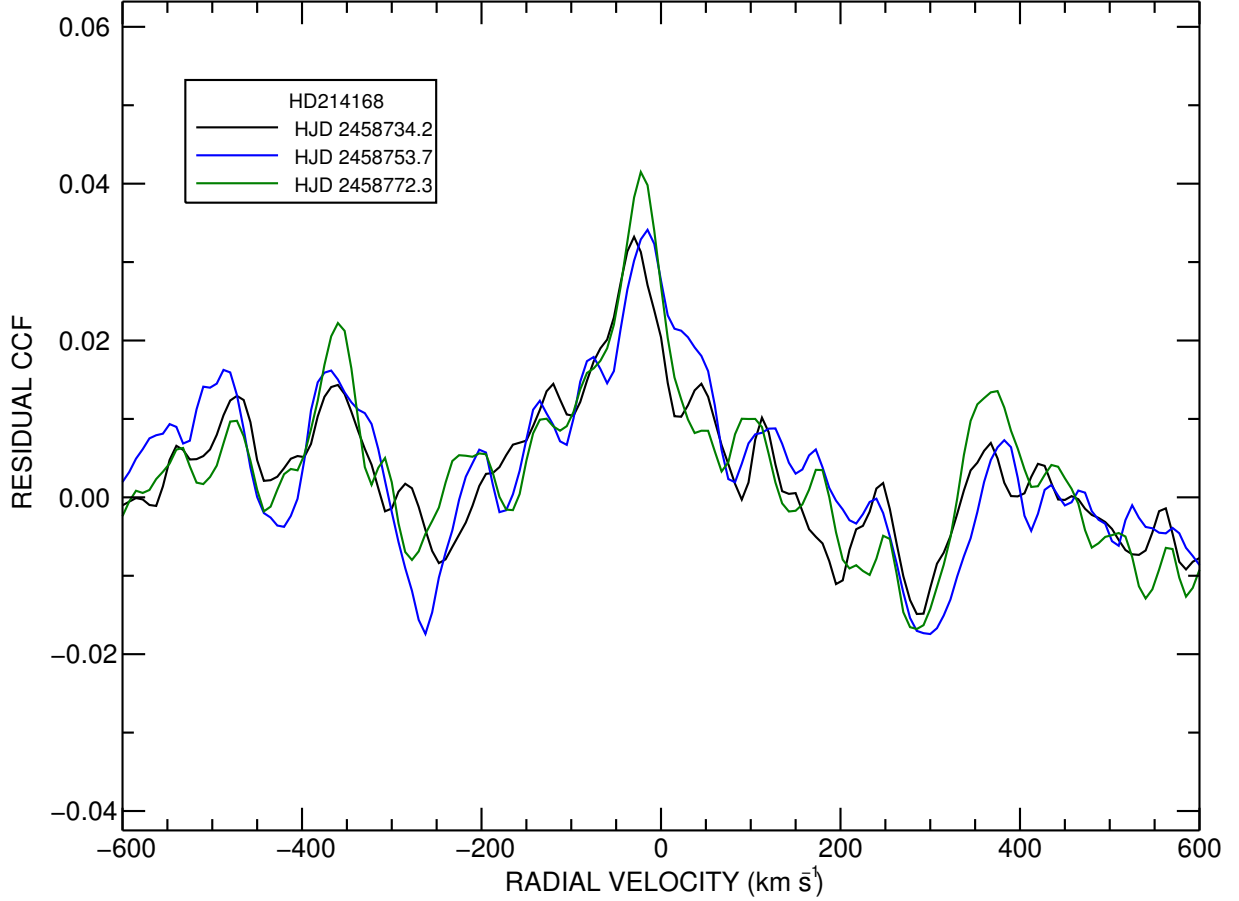


Figure 18. CCF residual plot of HD 214168 made through correlation with a cool model spectrum with $T_{\text{eff}} = 23.3$ kK.

We fit the SED of HD 214168 by assuming that the third (faintest) *HST*/STIS spectrum has a flux representative of the Be star alone, and then we adjusted the observed Johnson *UBV* magnitudes to give the Be star (assumed component Aa) magnitude by adding 0.56 ± 0.04 mag (assuming no significant color difference between Aa and Ab). The fit of the SED together with the Gaia DR2 distance yields a stellar radius of $6.0 \pm 1.1 R_{\odot}$ for Aa. The radius of Ab from the optical magnitude difference is then $4.9 \pm 0.9 R_{\odot}$ or somewhat larger if Ab is cooler than Aa. We caution that these values may be slightly overestimated because the FUV flux recorded in the third *HST*/STIS spectrum may include a small contribution from Ab.

Wang et al. (2018) were able to measure a CCF peak for an sdO companion in 9 of the 20 *IUE* spectra they analysed. This suggests that there are temporal variations that influence the visibility of the sdO star’s photospheric flux, as found in the case of HD 191610. Thus, the non-detection in

the CCFs from the *HST*/STIS spectra may be due to the making of the observations at a time when the sdO star was obscured from view.

REFERENCES

- Bailer-Jones, C. A. L., Rybizki, J., Fouesneau, M., Mantelet, G., & Andrae, R. 2018, *AJ*, 156, 58, doi: [10.3847/1538-3881/aacb21](https://doi.org/10.3847/1538-3881/aacb21)
- Becker, J. C., Johnson, J. A., Vand erburg, A., & Morton, T. D. 2015, *ApJS*, 217, 29, doi: [10.1088/0067-0049/217/2/29](https://doi.org/10.1088/0067-0049/217/2/29)
- Bodensteiner, J., Shenar, T., & Sana, H. 2020a, *A&A*, 641, A42, doi: [10.1051/0004-6361/202037640](https://doi.org/10.1051/0004-6361/202037640)
- Bodensteiner, J., Shenar, T., Mahy, L., et al. 2020b, *A&A*, 641, A43, doi: [10.1051/0004-6361/202038682](https://doi.org/10.1051/0004-6361/202038682)
- Boubert, D., & Evans, N. W. 2018, *MNRAS*, 477, 5261, doi: [10.1093/mnras/sty980](https://doi.org/10.1093/mnras/sty980)
- Bourgés, L., Lafrasse, S., Mella, G., et al. 2014, in *Astronomical Society of the Pacific Conference Series*, Vol. 485, *Astronomical Data Analysis Software and Systems XXIII*, ed. N. Manset & P. Forshay, 223
- Chojnowski, S. D., Wisniewski, J. P., Whelan, D. G., et al. 2017, *AJ*, 153, 174, doi: [10.3847/1538-3881/aa64ce](https://doi.org/10.3847/1538-3881/aa64ce)
- Chojnowski, S. D., Labadie-Bartz, J., Rivinius, T., et al. 2018, *ApJ*, 865, 76, doi: [10.3847/1538-4357/aad964](https://doi.org/10.3847/1538-4357/aad964)
- Colina, L., Bohlin, R., & Castelli, F. 1996, *HST Instrument Science Report CAL/SCS-008* (Baltimore: STScI)
- Costado, M. T., Alfaro, E. J., González, M., & Sampedro, L. 2017, *MNRAS*, 465, 3879, doi: [10.1093/mnras/stw2967](https://doi.org/10.1093/mnras/stw2967)
- Dachs, J., Hummel, W., & Hanuschik, R. W. 1992, *A&AS*, 95, 437
- Dachs, J., Hanuschik, R., Kaiser, D., et al. 1986, *A&AS*, 63, 87
- de Mink, S. E., Sana, H., Langer, N., Izzard, R. G., & Schneider, F. R. N. 2014, *ApJ*, 782, 7, doi: [10.1088/0004-637X/782/1/7](https://doi.org/10.1088/0004-637X/782/1/7)
- El-Badry, K., & Quataert, E. 2021, *MNRAS*, 502, 3436, doi: [10.1093/mnras/stab285](https://doi.org/10.1093/mnras/stab285)
- Eldridge, J. J., Fraser, M., Smartt, S. J., Maund, J. R., & Crockett, R. M. 2013, *MNRAS*, 436, 774, doi: [10.1093/mnras/stt1612](https://doi.org/10.1093/mnras/stt1612)
- Eldridge, J. J., Stanway, E. R., Xiao, L., et al. 2017, *PASA*, 34, e058, doi: [10.1017/pasa.2017.51](https://doi.org/10.1017/pasa.2017.51)
- ESA. 1997, *ESA Special Publication*, Vol. 1200, *The HIPPARCOS and TYCHO catalogues. Astrometric and photometric star catalogues derived from the ESA HIPPARCOS Space Astrometry Mission* (Noordwijk, Netherlands: ESA)
- Fitzpatrick, E. L. 1999, *PASP*, 111, 63, doi: [10.1086/316293](https://doi.org/10.1086/316293)
- Gies, D. R., Bagnuolo, William G., J., Ferrara, E. C., et al. 1998, *ApJ*, 493, 440, doi: [10.1086/305113](https://doi.org/10.1086/305113)
- Gies, D. R., & Wang, L. 2020, *ApJL*, 898, L44, doi: [10.3847/2041-8213/aba51c](https://doi.org/10.3847/2041-8213/aba51c)
- Gontcharov, G. A., & Mosenkov, A. V. 2018, *VizieR Online Data Catalog*, II/354
- Götberg, Y., de Mink, S. E., Groh, J. H., et al. 2018, *A&A*, 615, A78, doi: [10.1051/0004-6361/201732274](https://doi.org/10.1051/0004-6361/201732274)
- Götberg, Y., de Mink, S. E., Groh, J. H., Leitherer, C., & Norman, C. 2019, *A&A*, 629, A134, doi: [10.1051/0004-6361/201834525](https://doi.org/10.1051/0004-6361/201834525)
- Halbedel, E. M. 1996, *PASP*, 108, 833, doi: [10.1086/133804](https://doi.org/10.1086/133804)
- Han, Z., Podsiadlowski, P., & Lynas-Gray, A. 2010, *Ap&SS*, 329, 41, doi: [10.1007/s10509-010-0348-4](https://doi.org/10.1007/s10509-010-0348-4)
- Harmanec, P., Lipták, J., Koubský, P., et al. 2020, *A&A*, 639, A32, doi: [10.1051/0004-6361/202037964](https://doi.org/10.1051/0004-6361/202037964)
- Hartkopf, W. I., Mason, B. D., McAlister, H. A., et al. 1996, *AJ*, 111, 936, doi: [10.1086/117841](https://doi.org/10.1086/117841)
- Heber, U. 2009, *ARA&A*, 47, 211, doi: [10.1146/annurev-astro-082708-101836](https://doi.org/10.1146/annurev-astro-082708-101836)
- . 2016, *PASP*, 128, 082001, doi: [10.1088/1538-3873/128/966/082001](https://doi.org/10.1088/1538-3873/128/966/082001)
- Heber, U., Werner, K., & Drilling, J. S. 1988, *A&A*, 194, 223
- Hohle, M. M., Neuhäuser, R., & Schutz, B. F. 2010, *Astronomische Nachrichten*, 331, 349, doi: [10.1002/asna.200911355](https://doi.org/10.1002/asna.200911355)
- Howarth, I. D. 1987, *MNRAS*, 226, 249, doi: [10.1093/mnras/226.1.249](https://doi.org/10.1093/mnras/226.1.249)

- Huang, W., & Gies, D. R. 2006, *ApJ*, 648, 580, doi: [10.1086/505782](https://doi.org/10.1086/505782)
- Huang, W., Gies, D. R., & McSwain, M. V. 2010, *ApJ*, 722, 605, doi: [10.1088/0004-637X/722/1/605](https://doi.org/10.1088/0004-637X/722/1/605)
- Irrgang, A., Geier, S., Kreuzer, S., Pelisoli, I., & Heber, U. 2020, *A&A*, 633, L5, doi: [10.1051/0004-6361/201937343](https://doi.org/10.1051/0004-6361/201937343)
- Jaschek, M., & Egret, D. 1982, in *IAU Symposium*, Vol. 98, *Be Stars*, ed. M. Jaschek & H. G. Groth, 261
- Jilinski, E., Ortega, V. G., Drake, N. A., & de la Reza, R. 2010, *ApJ*, 721, 469, doi: [10.1088/0004-637X/721/1/469](https://doi.org/10.1088/0004-637X/721/1/469)
- Kaltcheva, N. 2009, *PASP*, 121, 1045, doi: [10.1086/606037](https://doi.org/10.1086/606037)
- Kervella, P., Arenou, F., Mignard, F., & Thévenin, F. 2019, *A&A*, 623, A72, doi: [10.1051/0004-6361/201834371](https://doi.org/10.1051/0004-6361/201834371)
- Kimble, R. A., Woodgate, B. E., Bowers, C. W., et al. 1998, *ApJL*, 492, L83, doi: [10.1086/311102](https://doi.org/10.1086/311102)
- Koubský, P., Kotková, L., Votruba, V., Šlechta, M., & Dvořáková, Š. 2012, *A&A*, 545, A121, doi: [10.1051/0004-6361/201219679](https://doi.org/10.1051/0004-6361/201219679)
- Koubský, P., Kotková, L., Kraus, M., et al. 2014, *A&A*, 567, A57, doi: [10.1051/0004-6361/201424022](https://doi.org/10.1051/0004-6361/201424022)
- Kozok, J. R. 1985, *A&AS*, 62, 7
- Krełowski, J., Galazutdinov, G. A., Strobel, A., & Bondar, A. 2017, *AcA*, 67, 281, doi: [10.32023/0001-5237/67.3.6](https://doi.org/10.32023/0001-5237/67.3.6)
- Langer, N., Baade, D., Bodensteiner, J., et al. 2020, *A&A*, 633, A40, doi: [10.1051/0004-6361/201936736](https://doi.org/10.1051/0004-6361/201936736)
- Lanz, T., & Hubeny, I. 2003, *ApJS*, 146, 417, doi: [10.1086/374373](https://doi.org/10.1086/374373)
- . 2007, *ApJS*, 169, 83, doi: [10.1086/511270](https://doi.org/10.1086/511270)
- Levenhagen, R. S., & Leister, N. V. 2006, *VizieR Online Data Catalog*, *J/MNRAS*/371/252
- Liu, J., Zhang, H., Howard, A. W., et al. 2019, *Nature*, 575, 618, doi: [10.1038/s41586-019-1766-2](https://doi.org/10.1038/s41586-019-1766-2)
- Liu, J., Zheng, Z., Soria, R., et al. 2020, *ApJ*, 900, 42, doi: [10.3847/1538-4357/aba49e](https://doi.org/10.3847/1538-4357/aba49e)
- Lopes de Oliveira, R., & Motch, C. 2011, *ApJL*, 731, L6, doi: [10.1088/2041-8205/731/1/L6](https://doi.org/10.1088/2041-8205/731/1/L6)
- Markwardt, C. B. 2009, in *Astronomical Society of the Pacific Conference Series*, Vol. 411, *Astronomical Data Analysis Software and Systems XVIII*, ed. D. A. Bohlender, D. Durand, & P. Dowler, 251. <https://arxiv.org/abs/0902.2850>
- McAlister, H. A., Hartkopf, W. I., Hutter, D. J., Shara, M. M., & Franz, O. G. 1987, *AJ*, 93, 183, doi: [10.1086/114297](https://doi.org/10.1086/114297)
- Mennickent, R. E., & Vogt, N. 1991, *A&A*, 241, 159
- Mermilliod, J. C. 1987, *A&AS*, 71, 413
- . 2006, *VizieR Online Data Catalog*, II/168
- Mourard, D., Monnier, J. D., Meilland, A., et al. 2015, *A&A*, 577, A51, doi: [10.1051/0004-6361/201425141](https://doi.org/10.1051/0004-6361/201425141)
- Peters, G. J., Gies, D. R., Grundstrom, E. D., & McSwain, M. V. 2008, *ApJ*, 686, 1280, doi: [10.1086/591145](https://doi.org/10.1086/591145)
- Peters, G. J., Pewett, T. D., Gies, D. R., Touhami, Y. N., & Grundstrom, E. D. 2013, *ApJ*, 765, 2, doi: [10.1088/0004-637X/765/1/2](https://doi.org/10.1088/0004-637X/765/1/2)
- Peters, G. J., Wang, L., Gies, D. R., & Grundstrom, E. D. 2016, *ApJ*, 828, 47, doi: [10.3847/0004-637X/828/1/47](https://doi.org/10.3847/0004-637X/828/1/47)
- Pols, O. R., Cote, J., Waters, L. B. F. M., & Heise, J. 1991, *A&A*, 241, 419
- Prša, A., Harmanec, P., Torres, G., et al. 2016, *AJ*, 152, 41, doi: [10.3847/0004-6256/152/2/41](https://doi.org/10.3847/0004-6256/152/2/41)
- Rauch, T. 1993, *A&A*, 276, 171
- Rauch, T., Heber, U., Hunger, K., Werner, K., & Neckel, T. 1991, *A&A*, 241, 457
- Riley, A., Biretta, J., Hernandez, S., & et al. 2019, *STIS Instrument Handbook for Cycle 28*, Version 18.0 (Baltimore: STScI)
- Rivinius, T., Baade, D., Hadrava, P., Heida, M., & Klement, R. 2020, *A&A*, 637, L3, doi: [10.1051/0004-6361/202038020](https://doi.org/10.1051/0004-6361/202038020)
- Sana, H., de Mink, S. E., de Koter, A., et al. 2012, *Science*, 337, 444, doi: [10.1126/science.1223344](https://doi.org/10.1126/science.1223344)
- Schootemeijer, A., Götberg, Y., de Mink, S. E., Gies, D., & Zapartas, E. 2018, *A&A*, 615, A30, doi: [10.1051/0004-6361/201731194](https://doi.org/10.1051/0004-6361/201731194)
- Shafter, A. W., Szkody, P., & Thorstensen, J. R. 1986, *ApJ*, 308, 765, doi: [10.1086/164549](https://doi.org/10.1086/164549)
- Shao, Y., & Li, X.-D. 2014, *ApJ*, 796, 37, doi: [10.1088/0004-637X/796/1/37](https://doi.org/10.1088/0004-637X/796/1/37)
- Shenar, T., Bodensteiner, J., Abdul-Masih, M., et al. 2020, *A&A*, 639, L6, doi: [10.1051/0004-6361/202038275](https://doi.org/10.1051/0004-6361/202038275)

- Slettebak, A. 1982, *ApJS*, 50, 55,
doi: [10.1086/190820](https://doi.org/10.1086/190820)
- Slettebak, A., Wagner, R. M., & Bertram, R.
1997, *PASP*, 109, 1, doi: [10.1086/133852](https://doi.org/10.1086/133852)
- Sohn, S. T., Boestrom, K. A., Proffitt, C., & et al.
2019, *STIS Data Handbook*, Version 7.0
(Baltimore: STScI)
- Tauris, T. M., Kramer, M., Freire, P. C. C., et al.
2017, *ApJ*, 846, 170,
doi: [10.3847/1538-4357/aa7e89](https://doi.org/10.3847/1538-4357/aa7e89)
- Thaller, M. L., Bagnuolo, Jr., W. G., Gies, D. R.,
& Penny, L. R. 1995, *ApJ*, 448, 878,
doi: [10.1086/176016](https://doi.org/10.1086/176016)
- Thompson, G. I., Nandy, K., Jamar, C., et al.
1978, *Catalogue of stellar ultraviolet fluxes: a
compilation of absolute stellar fluxes measured
by the Sky Survey Telescope (S2/68) aboard
the ESRO satellite TD-1 (The Science Research
Council)*
- Tokovinin, A., Everett, M. E., Horch, E. P.,
Torres, G., & Latham, D. W. 2019, *AJ*, 158,
167, doi: [10.3847/1538-3881/ab4137](https://doi.org/10.3847/1538-3881/ab4137)
- van Leeuwen, F. 2007, *A&A*, 474, 653,
doi: [10.1051/0004-6361:20078357](https://doi.org/10.1051/0004-6361:20078357)
- Wade, R. A., & Rucinski, S. M. 1985, *A&AS*, 60,
471
- Wang, L., Gies, D. R., & Peters, G. J. 2017, *ApJ*,
843, 60, doi: [10.3847/1538-4357/aa740a](https://doi.org/10.3847/1538-4357/aa740a)
- . 2018, *ApJ*, 853, 156,
doi: [10.3847/1538-4357/aaa4b8](https://doi.org/10.3847/1538-4357/aaa4b8)
- Wellstein, S., Langer, N., & Braun, H. 2001, *A&A*,
369, 939, doi: [10.1051/0004-6361:20010151](https://doi.org/10.1051/0004-6361:20010151)
- Yudin, R. V. 2001, *A&A*, 368, 912,
doi: [10.1051/0004-6361:20000577](https://doi.org/10.1051/0004-6361:20000577)
- Zorec, J., Frémat, Y., Domiciano de Souza, A.,
et al. 2016, *A&A*, 595, A132,
doi: [10.1051/0004-6361/201628760](https://doi.org/10.1051/0004-6361/201628760)
- Zucker, S. 2003, *MNRAS*, 342, 1291,
doi: [10.1046/j.1365-8711.2003.06633.x](https://doi.org/10.1046/j.1365-8711.2003.06633.x)